

For Reference

NOT TO BE TAKEN FROM THIS ROOM

For Reference

NOT TO BE TAKEN FROM THIS ROOM

EX LIBRIS
UNIVERSITATIS
ALBERTAENSIS



THE UNIVERSITY OF ALBERTA

THE BOUND STATES OF Na^{21} VIA
THE $\text{Ne}^{20}(\text{d}, \text{n})\text{Na}^{21}$ REACTION

by



Max Blake Burbank

A THESIS

SUBMITTED TO THE FACULTY OF GRADUATE STUDIES
IN PARTIAL FULFILMENT OF THE REQUIREMENTS FOR THE DEGREE
OF MASTER OF SCIENCE

DEPARTMENT OF PHYSICS

EDMONTON, ALBERTA

September, 1967

UNIVERSITY OF ALBERTA
FACULTY OF GRADUATE STUDIES

The undersigned certify that they have read, and recommend to the Faculty of Graduate Studies for acceptance, a thesis entitled THE BOUND STATES OF Na^{21} VIA THE $\text{Ne}^{20} (d,n)\text{Na}^{21}$ REACTION, submitted by Max Blake Burbank in partial fulfilment of the requirements for the degree of Master of Science.

ACKNOWLEDGEMENTS

I would like to thank my supervisors: Dr. G. C. Neilson for suggesting this project and Dr. W. J. McDonald for his continued interest and assistance in bringing about its fruition in Dr. Neilson's absence. Particular thanks are due Dr. McDonald for his invaluable assistance in setting up and operating the electronics.

I would also like to extend my thanks to Mr. T. B. Grandy for his contributions to the Associated Particle Experiment and to Mr. G. Frank for his continued assistance in performing both the Associated Particle and $\text{Ne}^{20}(\text{d},\text{n})\text{Na}^{21}$ experiments.

Appreciation is also extended to Mr. J. F. Easton for writing the program, ASPANL.

Acknowledgement is also extended to Mr. J. B. Elliot, Mr. L. Holm, Mr. N. Riebeek, and Mr. C. Green for their work in this research.

Credit is also due Mrs. Lee Watson for her patience and effort in typing the thesis.

Finally I would like to thank the National Research Council and the University of Alberta for their financial support during the course of this research.

ABSTRACT

An experimental technique is developed for measuring absolute neutron detection efficiencies and subsequently used in the structure study of Na^{21} via the $\text{Ne}^{20}(\text{d},\text{n})\text{Na}^{21}$ reaction.

Angular distributions of the neutrons leading to the four bound states of Na^{21} were obtained at a deuteron bombarding energy of 3.924 MeV. A D.W.B.A. analysis was used to check the spin and parity assignments and to obtain absolute spectroscopic factors for the Na^{21} 0.335 ($5/2^+$), 1.751 ($7/2^+$), and 2.433 ($1/2^+$) levels.

A strong coupling collective model interpretation of the Na^{21} level structure is given and a band-limited summation rule is used to estimate the compound reaction contribution to the formation of the 0.335, 1.751, and 2.433 MeV. levels.

ACKNOWLEDGEMENTS

I would like to thank my supervisors: Dr. G. C. Neilson for suggesting this project and Dr. W. J. McDonald for his continued interest and assistance in bringing about its fruition in Dr. Neilson's absence. Particular thanks are due Dr. McDonald for his invaluable assistance in setting up and operating the electronics.

I would also like to extend my thanks to Mr. T. B. Grandy for his contributions to the Associated Particle Experiment and to Mr. G. Frank for his continued assistance in performing both the Associated Particle and $\text{Ne}^{20}(\text{d},\text{n})\text{Na}^{21}$ experiments.

Appreciation is also extended to Mr. J. F. Easton for writing the program, ASPANL.

Acknowledgement is also extended to Mr. J. B. Elliot, Mr. L. Holm, Mr. N. Riebeek, and Mr. C. Green for their work in this research.

Credit is also due Mrs. Lee Watson for her patience and effort in typing the thesis.

Finally I would like to thank the National Research Council and the University of Alberta for their financial support during the course of this research.

TABLE OF CONTENTS

	Page
CHAPTER I INTRODUCTION	1
CHAPTER II EXPERIMENTAL DETAILS	4
2.1 Introduction	4
2.2 Beam Transport System	6
2.3 Time of Flight Electronics	8
2.4 Gas Target	11
CHAPTER III NEUTRON DETECTOR EFFICIENCY MEASUREMENTS	14
3.1 The Relative Efficiency Experiment	14
3.2 The Absolute Efficiency Experiment	16
(i) Introduction	16
(ii) The Gas Target Assembly	17
(iii) Construction of the Formvar Window	21
(iv) Electronics of the Associated Particle Experiment	24
3.3 Presentation of Results	27
3.4 Conclusion	30
CHAPTER IV THE $\text{Ne}^{20}(\text{d},\text{n})\text{Na}^{21}$ REACTION	32
4.1 Introduction	32
4.2 The Experiment	35
4.3 The D.W.B.A. Analysis of the $\text{Ne}^{20}(\text{d},\text{n})\text{Na}^{21}$ Reaction	44
(i) D.W.B.A. Theory	44

	(ii) The D.W.B.A. Angular Distributions	57
4.4	Discussion	62
	(i) Approximations made in the D.W.B.A. Analysis	62
	(ii) The absence of stripping structure in the formation of the ground state of Na^{21}	64
	(iii) Collective Model interpretation of Na^{21}	65
APPENDIX A	ASSOCIATED PARTICLE ANALYSIS: ASPANL	A-1
A-1	Introduction	A-1
A-2	Data Input	A-4
A-3	Data Output	A-11

LIST OF FIGURES

		Following page
2-1	Block Diagram of Beam Transport System	6
2-2	Time of Flight Electronics	8
2-3	Gas Target Cell	11
3-1	Gas Target	18
3-2	Redesign of Gas Cell	20
3-3	Apparatus for Rolling Foils	21
3-4	Associated Particle Electronics	24
3-5	Associated Particle Spectrum	26
3-6	Na^{22} γ -Ray Spectrum	27
3-7	Neutron Detector Efficiency Response	29
4-1	Level Structure of Ne^{21} and Na^{21}	32
4-2	Neutron Time Spectrum	36
4-3	Yield Curves	43
4-4	$\text{Ne}^{20}(\text{d},\text{d})\text{Ne}^{20}$ Elastic Scattering	59
4-5	Neutron Angular Distributions	59
4-6	Nilsson Diagram	68
A-1	Associated Particle Geometry	A-1
A-2	Output Data Sheet	A-11
A-3	Scatter Diagram	A-11
A-4	Flux Contour	A-11

CHAPTER I

INTRODUCTION

In low energy nuclear spectroscopy one has two basic interests. One is to elucidate the structural content of the nucleus of interest, and the other is to determine the nature of the reaction mechanism. Progress in both these areas is governed by the extent to which a comparison can be made between one's experimental findings and various model predictions.

A number of important nuclear parameters, such as spin, parity, and excitation energy can generally be determined on the basis of relative cross section data. However, these parameters tend to represent the more gross features of the nucleus and provide only limited insight into its internal make up. As one attempts to probe more deeply into, not only the internal makeup of the nucleus but also into the nature of the reaction mechanism, a more quantitative analysis is required. That is, only through absolute cross section data can one attempt to answer questions such as:

- (i) to what extent is the residual nucleus represented by the target nucleus plus the captured particle;

(ii) to what extent can the nucleon-nucleon interactions be represented by averaged potentials; and

(iii) to what extent is there competition between the direct reaction and compound reaction mechanisms?

All three questions relate directly to the two fundamental problems in nuclear physics: that of determining the nature of the nuclear forces, and that of treating the many body problem.

In this thesis a report is given of work undertaken at the University of Alberta to: (i) develop an experimental technique for measuring absolute neutron detection efficiencies and (ii) apply the results of such a technique to the absolute cross-section, structure study of Na^{21} via the $\text{Ne}^{20}(\text{d},\text{n})\text{Na}^{21}$ reaction.

For the absolute efficiency measurement the $\text{D}(\text{d},\text{n})\text{He}^3$ reaction was used, with the He^3 particles being detected in coincidence with their associated neutrons. The coincidence requirements were such that a neutron was detected if and only if an associated He^3 particle was also detected. However, all He^3 particles were detected independent of their associated neutrons. The ratio between the number of neutrons detected to the number of He^3 particles is then a measure of the absolute neutron detection efficiency.

The study of the $\text{Ne}^{20}(\text{d},\text{n})\text{Na}^{21}$ reaction was initiated as a search for new low lying structure within the Na^{21} nucleus

(viz. a questionable 1.42 MeV level (Ma 56) and possible doublet structure in the 0.335 (Gi 65) and 2.433 (Po 67) levels) and to obtain absolute cross section data for the formation of the four bound states of Na^{21} (i.e.: ground ($3/2^+$), 0.335 MeV ($5/2^+$), 1.751 MeV ($7/2^+$), and 2.433 MeV ($1/2^+$) levels). The Ne^{20} target consisted of a nickel-windowed gas cell and the neutrons were detected via a time-of-flight technique. Both structure and reaction interpretations of the Na^{21} nucleus are made within the framework of the strong coupling collective model.

CHAPTER II

EXPERIMENTAL DETAILS

2.1 Introduction

As a consequence of the neutron's neutral charge there is no unambiguous relationship between the recoil pulse height spectrum of a neutron scintillator and the energy of the incident neutron. Thus, to date, the most precise method of measuring neutron energies is to determine particle velocities by individually timing their flight over an accurately known distance. Such a technique requires the accurate determination of two time points corresponding to the generation and detection of the neutron. These time points are most accurately determined by using a pulsed beam in conjunction with fast timing circuits. Such a technology, in recent years, has developed into a very powerful tool available for fast neutron spectroscopy in the nano-second time scale. The significant features are:

- (i) good energy resolution
- (ii) high detection efficiency
- (iii) applicability to a wide range of neutron energies.

The start signal originates from a pick off capacitor located within the beam tube next to the target. The beam pulse induces a charge which is amplified and shaped appropriately.

The corresponding stop signal originates from the neutron detector, which consists of an organic scintillator optically coupled to a photomultiplier tube.

The start-stop signals are then fed into a fast time-to-amplitude converter and the corresponding output signal is analyzed by a multichannel pulse height analyzer.

The length of the beam pulses are short in comparison to the corresponding neutron flight times. This serves to maximize energy resolution which, for non-relativistic neutrons, is given by

$$\frac{\Delta E}{E} = 2 \frac{\Delta t}{t} , \quad (2.1-1)$$

(where Δt is the width of the pulse, t the flight time of the neutron, E the energy of the neutron, and ΔE the resulting uncertainty in the neutron energy.) In addition the pulse repetition rate is sufficiently slow to allow the low energy neutrons to be detected before the arrival of the next pulse.

For the system employed at the University of Alberta an intrinsic pulse width of less than 0.5 ns. is obtainable at a repetition rate of 1 mH. The neutron flight path is variable

from 1 to 6 meters. And the multichannel pulse height analyzer consists, in part, of an on line SDS-920 computer.

2.2 Beam Transport System

Fig. 2-1 is a schematic representation of the beam transport system used at the University of Alberta for the generation of a high intensity pulsed beam. The system employs both pre-acceleration pulsing and post-acceleration compression, a combination that serves to maximize the beam current without increasing the pulse width.

A d.c. beam of several milliamps is generated, within a source bottle, at the high voltage terminal of the Van de Graaff¹⁾ by a 125 mH. source oscillator in conjunction with a source magnet. The beam is brought out through an opening known as the canal and focused, by a set of Einzel lens and a terminal analyzing magnet, at a 1/16 inch aperture. Pre-acceleration pulsing is achieved by sweeping the beam, in an elliptical pattern, over the 1/16 inch aperture by a pair of R.F. deflection plates set at right angles to each other and with their voltages 90° out of phase. The R.F. frequency is set at 1 mH. producing a triangular pulse of 10 to 15 ns. pulse width. Additional focusing is achieved by another lens, the self focusing column, and a quadruple doublet.

¹⁾ A 6.00 MeV Van de Graaff Accelerator, Model CN, High Voltage Engineering Corp., Burlington, Massachusetts, U.S.A.

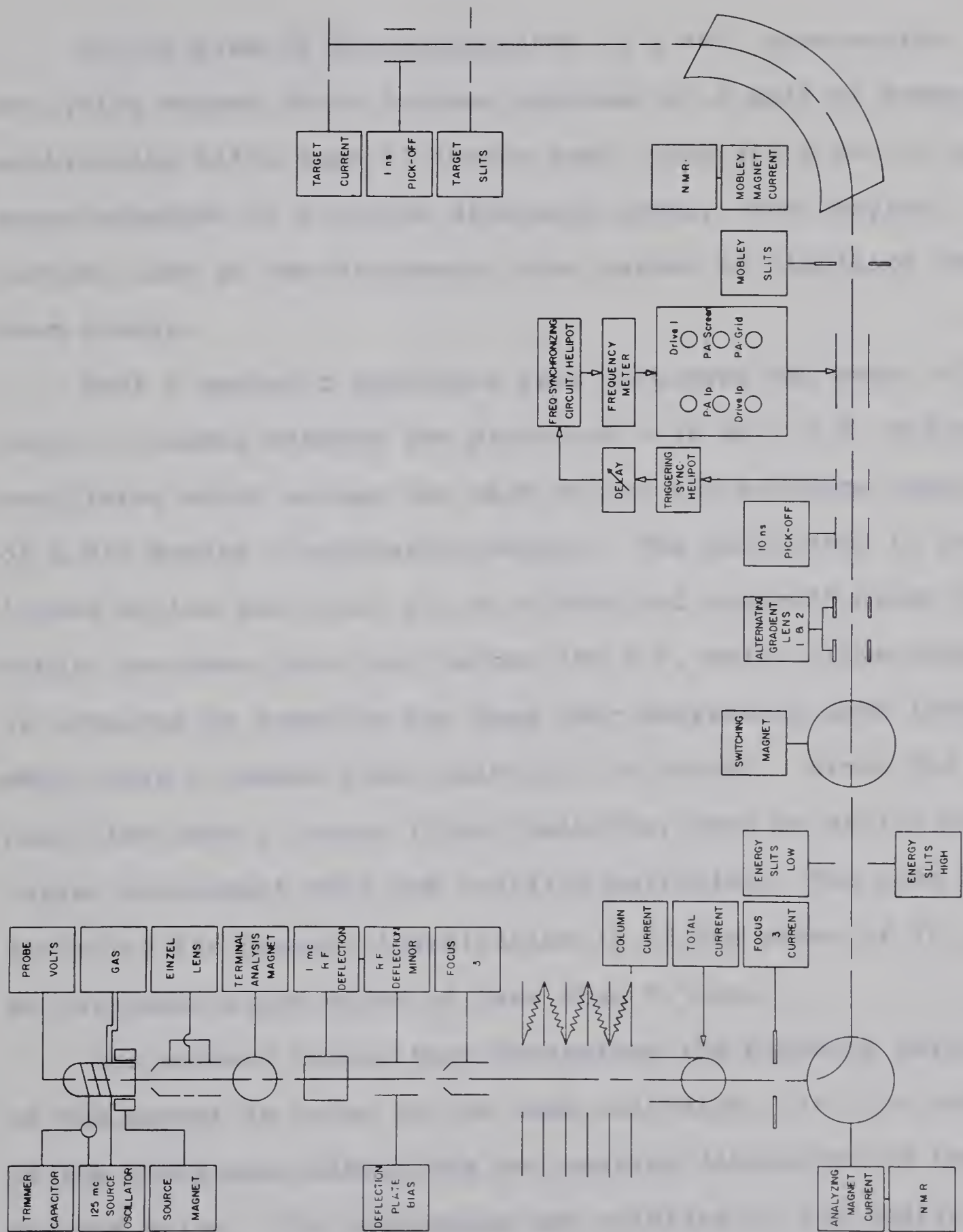


FIGURE 2-1: BLOCK DIAGRAM OF BEAM TRANSPORT SYSTEM

At the base of the accelerator is a 90° mass-energy analyzing magnet which focuses the beam at a pair of energy stabilizing slits some 57 inches away. The slits are in turn ~~servo~~-connected to a corona discharge probe. The varying current load of the discharge probe serves to stabilize the beam energy.

Next a magnetic quadrupole lens refocuses the beam, after which it passes between the plates of a 10 mH., R.F. deflection oscillator which sweeps the beam across the entrance aperture of a 90° Mobley compression magnet. The oscillator is phase locked to the ion burst via a cylindrical pick-off probe placed within the beam tube just before the R.F. unit. Time compression is achieved by sweeping the beam over decreasing path lengths which have a common focal point at the target. Since the leading particles have a longer flight path they tend to arrive at the target coincident with the trailing particles. The beam bunching factor of the present installation is of the order of 12, giving an intrinsic pulse width of less than 0.5 ns.

The primary factor that determines the bunching performance of the magnet is known as the beam emittance. It is a measure of the transverse dimensions and angular divergence of the pre-bunched pulse. Its importance and relation to the design criteria of the Mobley magnet are discussed in detail in the Ph.D. thesis of W. G. Davies (Da 66).

2.3 Time of Flight Electronics

Fig. 2.2 is a schematic representation of the electronics making up the time-of-flight spectrometer. Parallel to the main detector is a monitor system from which a normalization factor is obtained for angular distribution studies.

The main detector consists of a Philips XP 1040 photomultiplier tube optically coupled to a cylindrical (3.45" x 0.75") quartz container filled with Ne 213¹⁾ liquid scintillator. The monitor detector consists of a Naton phosphor²⁾ optically coupled to a RCA 8575 photomultiplier tube.

The main detector is mounted on a movable cart which, under control from the console, can be positioned in both detection angle and flight path. The monitor is mounted on a tripod and generally held at a fixed position.

The stop signal, for both systems, comes from a 3 inch long cylindrical capacitor placed within the beam tube some 30 cm. in front of the target. Before reaching the stop channel of the time-to-amplitude converter (T.A.C.) the pulse is delayed sufficiently to allow a start pulse, corresponding to the lowest energy neutrons, to reach the T.A.C. first. By so inverting the time sequence one can decrease the overall dead time of the system. This is a consequence of the virtual elimination of those

¹⁾ Nuclear Enterprises Ltd., Winnipeg, Manitoba.

²⁾ Nash & Thompson, Ltd., Hookrise South, Tolworth, Surrey, England.

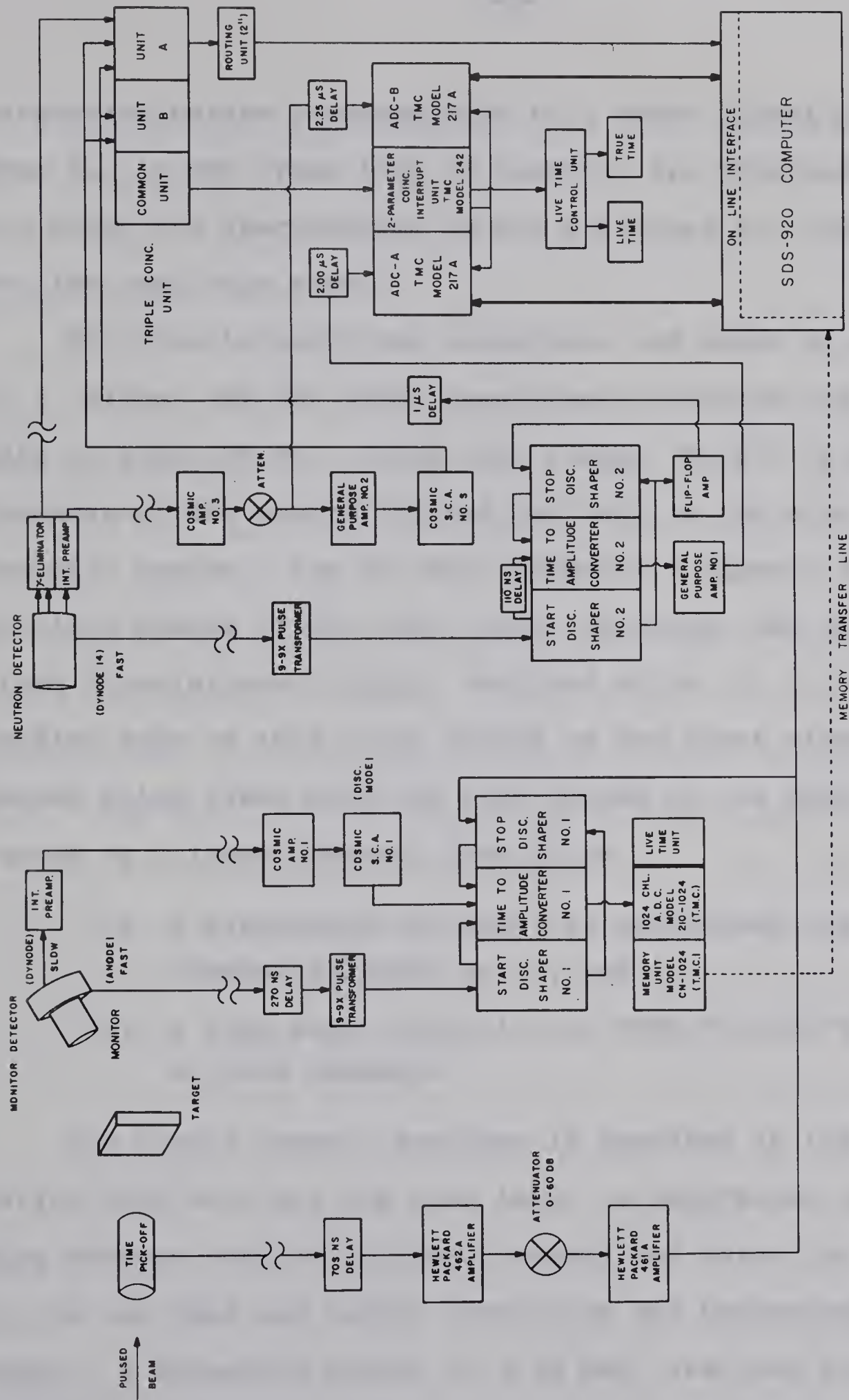


Fig. 2-2 Time Of Flight Electronics

saturation pulses corresponding to a start signal but no stop. That is, in the event that no neutrons are detected for a given ion burst the spectrometer is not activated but remains ready for the next beam burst.

The time-to-amplitude converters are based on a design by D. L. Wieber (Wi 63) using capacitance charging and a time base of about 300 ns. Cross over timing (Ge 67) is used in both channels of the monitor system but only in the stop channel of the main system. For the main detector a signal is taken from the 14th dynode of the photo tube, inverted, and fed into a start discriminator shaper, designed by Dr. G. C. Neilson. The leading edge of this pulse serves as the start signal. A second pulse taken from the 11th dynode of the photo tube serves as a linear channel from which

- (i) a discrimination level is determined via signal channel analyser No. 3, and
- (ii) a time base correction is made via ADC-B and the on line computer.

The single channel analyzer is operated in the discrimination mode only and the bias level is determined as a compromise between neutron threshold energy and detection efficiency on the one hand and energy resolution and background on the other. A threshold energy of 0.80 MeV. was used throughout this work.

The digital information entering the computer via ADC-B is a measure of the pulse height of the start signal activating T.A.C. No. 2. Since time zero is determined by when this pulse crosses a fixed bias level, varying time points will correspond to varying pulse heights. However, once having determined the relationship between pulse height and time shift the knowledge entering the computer via ADC-B allows one to correct for this time walk, resulting in an increase in resolution (0.9 ns. from 1.25 ns.).

Such a correction is achieved by a general purpose program (GPKS) written by Dr. W. K. Dawson. First the pulse height spectrum of a mono-energetic neutron peak is divided into 64 bins. The time shift for each bin is determined and entered as a table in the computer. Thus every pulse that enters the computer via ADC-B is associated with one of the 64 bins. The corresponding time correction is determined from the table and added to the timing data entering the computer via ADC-A.

Both analog to digital counters¹⁾, ADC-A and ADC-B are 1024 channel units, which along with the walk correction operation produces a system dead time of the order of 700 μ s. This allows a maximum conversion rate of about 1500 counts per second. During the time GPKS is handling data, input to the computer is inhibited by the coincidence interrupt unit. Its

¹⁾ Technical Measurement Corporation, Model 217A, North Haven, Conn., U. S. A.

detailed operation is discussed in an internal report by D. A. Gedcke (Ge 66).

Signals from the anode and 13th dynode of the photo tube provide inputs to a γ -ray, neutron discriminator of the pulse-overlap design (Re 66). The output, which signifies the identification of the pulse as a neutron is held in coincidence with signals validating it as being above the neutron threshold level and also initiating a legitimate start pulse. The output of the triple coincidence is then fed into a routing unit designed by D. A. Gedeke (Ge 66a) which routes the corresponding corrected timing data into a second 1024 channel memory range of the computer. The first 1024 channel range then contains those data that the n- γ discriminator identified as γ -rays.

In addition to storing, correcting, and displaying data the utility of GPKS allows one to transfer the memory contents of the T.M.C. 210 unit, which contains the associated monitor spectrum, to the memory of the computer. All data is then easily transferred to magnetic tape for storage purposes.

2.4 Gas Target

Fig. 2-3 is a design drawing of the gas target cell used throughout most of the $\text{Ne}^{20}(\text{d},\text{n})\text{Na}^{21}$ work.

The cell proper consists of a sheet of 0.010" tantalum folded into a rectangular parallelepiped of dimensions $1\frac{1}{4}"$ H. x 1" W. x $\frac{1}{4}"$ T. The enclosure is capped, top and

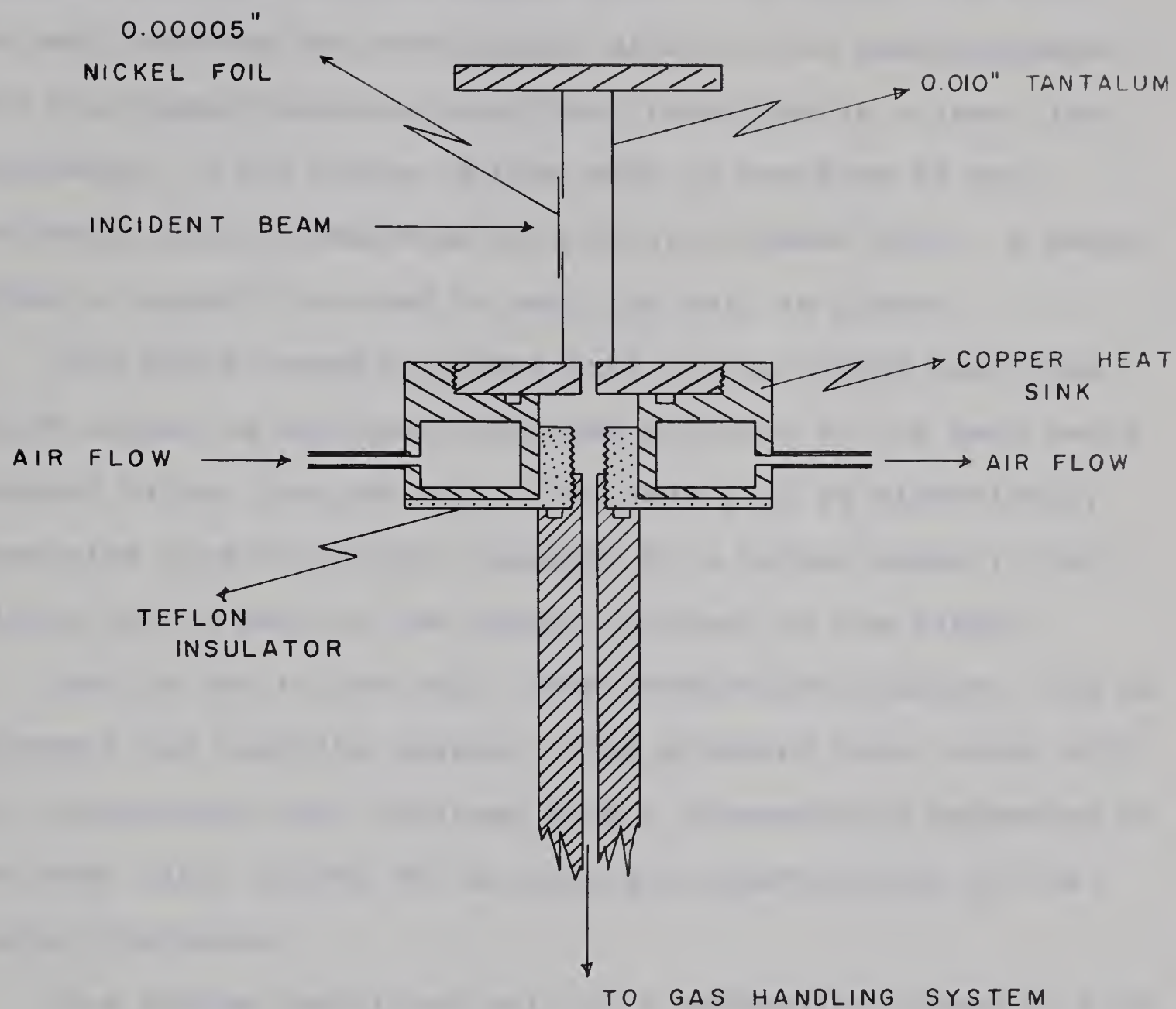


FIG. 2-3: GAS TARGET CELL

bottom, with two slotted copper discs. An epoxy¹⁾ is used to seal together the overlapping sides of the parallelepiped and the copper-tantalum interface, resulting in a leak tight enclosure. A 3/8" hole is then made in one face of the enclosure and covered over by a 50 μ in. nickel foil. A second grade of epoxy²⁾ is used to seal the foil in place.

The whole assembly screws into an air cooled heat sink which serves to dissipate the heat produced by the beam being stopped within the gas cell. The heat sink is electrically insulated from the target assembly by a teflon washer, which allows one to monitor the charge incident on the target.

Gas is fed to the cell, under controlled pressure, via an external gas handling system. This pressure data, along with the temperature data obtained from a thermocouple connected to the heat sink, allows for an accurate determination of the target thickness.

The system functioned well at a bombarding energy of 4.00 MeV., a gas pressure of 45 cm. of Hg., and a beam current of 1.5 μ amps with neither the nickel foil nor the tantalum backing contributing significantly to the background. However, when attempts were made to raise the bombarding energy to 5.00 MeV.

¹⁾ Plastic Steel, Devcon Canada Ltd.

²⁾ Epoxy Glue, Borden Chemical Co.

the foils continued to rupture. This was attributed to the system being unable to dissipate the heat fast enough, resulting in a high temperature and strain on the foil due to the difference in the thermal expansion coefficient of nickel and tantalum. A new design was then proposed for higher energy studies. It consisted of making a hole in both faces of the cell and catching the beam in a Faraday Cup. Preliminary work has shown the new design to be successful.

CHAPTER III

NEUTRON DETECTOR EFFICIENCY MEASUREMENTS

3.1 The Relative Efficiency Experiment

Fundamental to angular distribution studies is the ability to renormalize the raw data such that all parameters giving rise to a variation in count rate are removed, except that due to the differential cross section. Corrections for variations in target thickness, charge collection, and run time are achieved by placing a secondary detector at a fixed angle and normalizing the primary data to one of the peaks in the monitor spectrum. The correction for the variation in detector efficiency as a function of neutron energy is achieved by first evaluating the efficiency function. A number of experimental techniques have been employed at this laboratory, with varying degrees of success, in an effort to measure this function.

The initial approach was to use the $\text{Li}^7(\text{p},\text{n})\text{Be}^7$ reaction over a proton energy range of 2.5 to 5.0 MeV. This gives, at zero degrees, a neutron energy range of 0.786 to 3.331 MeV. In addition to the main detector the neutrons were detected by a "flat-response" long counter of the McKibben type (Al60)

placed along side the principal detector. The basic idea was to unfold the efficiency function by normalizing the counts of the main detector to those of the long counter. To make the measurement meaningful, however, one must account for the fact that the long counter sees neutrons from both the ground and first excited states of Be^7 (Be 61). Whereas, to establish a unique neutron energy, only the ground state peak of the principal counter is used. In addition, one must account for the known response of the long counter (Al 60).

When a detailed evaluation of the efficiency curve was measured in this way a number of anomalies, in the form of resonant humps, occurred around 2.5 MeV. In addition, the reproducibility of points was not very satisfactory.

In an effort to remove these anomalies the same technique was applied to the monoenergetic neutron sources of the $\text{C}^{12}(\text{He}^3, n)\text{O}^{14}$, $\text{C}^{13}(\alpha, n)\text{O}^{15}$, and $\text{T}(p, n)\text{He}^3$ reactions. However, the cross sections for the $\text{C}^{12}(\text{He}^3, n)\text{O}^{14}$ and $\text{C}^{13}(\alpha, n)\text{O}^{15}$ reactions proved to be too small, leading to a high background count in the long counter and consequently a very poor reproducibility of points.

The tritium target was of the zirconium backed variety and, due to the energy loss of the incident protons in penetrating the backing, gave rise to a neutron peak with a long low-energy tail (Fi 66). Specifically, the area of the tail varied from 12 to 20 percent of the total area. This then invalidated the

idea of a unique neutron energy and also made it difficult to establish a consistent background cut-off criterion.

The technique finally adopted, and that proved reasonably successful, consisted of an angular distribution study of the $T(p,n)He^3$ reaction at 3.00 MeV. and the $D(d,n)He^3$ reaction at 3.52 MeV. The efficiency curve was obtained by normalizing the experimental angular distributions to the published values for the respective reactions (Go 61), (Br 60). The $T(p,n)He^3$ reaction covered a neutron energy range from 0.728 to 2.62 MeV and the $D(d,n)He^3$ reaction from 2.31 to 6.79 MeV. Fig. 3-7 illustrates the relative efficiency curve obtained in this way.

3.2 The Absolute Efficiency Experiment

(i) Introduction

The basic inadequacy in all of the aforementioned techniques for measuring neutron detection efficiencies is their dependence on published data. To overcome this dependence and at the same time obtain absolute efficiencies of high reliability a project was initiated to measure detection efficiencies via the associated particle technique. The object of this technique is to measure the charged particle counterparts of a neutron producing reaction in coincidence with the neutrons. From the one to one relationship that results one can obtain absolute efficiencies by forming the ratio of the number of neutrons produced, as given by the charged particle counts, to the number of neutrons detected, as given by the neutron spectrometer.

In choosing a reaction compatible with the demands of this experiment, the following criteria were considered:

- (i) the reaction should produce neutrons within the energy range of interest (0.5 to 10.0 MeV.);
- (ii) the mass of the charged particle should be small so as to share a reasonably high fraction of the recoil energy;
- (iii) the reaction should be a monoenergetic neutron source; and
- (iv) to facilitate the escape of the charged particles the target material should be in gaseous form.

These conditions were most successfully satisfied by the $D(d,n)He^3$ reaction ($Q = 3.266$ MeV.) and a gas target.

(ii) The Gas Target Assembly

In addition to the judicious choice of a reaction, the absolute efficiency experiment required a rather unique target design. The principal requirements were:

- (i) facility for handling a gaseous target material within a vacuum environment;
- (ii) containing the deuterium gas in such a way and by such a material as to allow the He^3 particles to escape;
- (iii) provision for mounting and positioning a solid state detector and collimation system; and
- (iv) provision for aligning the target with respect to the incident beam.

In addition to fulfilling these requirements, consideration was given to a scheme designed to maximize the active life of the target. This consisted of a provision for rotating the gas cell, with respect to the incident beam, and thus reducing the weakening effect of the beam on the very thin membrane which served to contain the gas.

Fig. 3-1 is a relief drawing of the base assembly and gas target proper. This structure in turn fits up into an existing bell shaped enclosure positioned at the end of the Mobley compression magnet. When so positioned an O-ring seal on the upper face of the bottom flange (1) allows for the subsequent evacuation of the target chamber.

The cylindrical gas cell (2) was of the first generation design. It allowed for charged particle detection at all angles except for 5 degree cones at zero and 180 degrees. The gas within the cell was contained by an ultra-thin window of Formvar foil (3) which was stretched across an annular gap 0.200" high. The gap was maintained by two tungsten pegs (4) (0.090" in dia.) positioned 180 degrees apart. To facilitate collimation of the incident beam and to prevent it from hitting the brass cell, shields of 0.010" gold (5) were placed around the target and slightly overlapping the Formvar window.

The remainder of the target assembly consists of three concentric shafts, with the inner two being allowed to rotate.

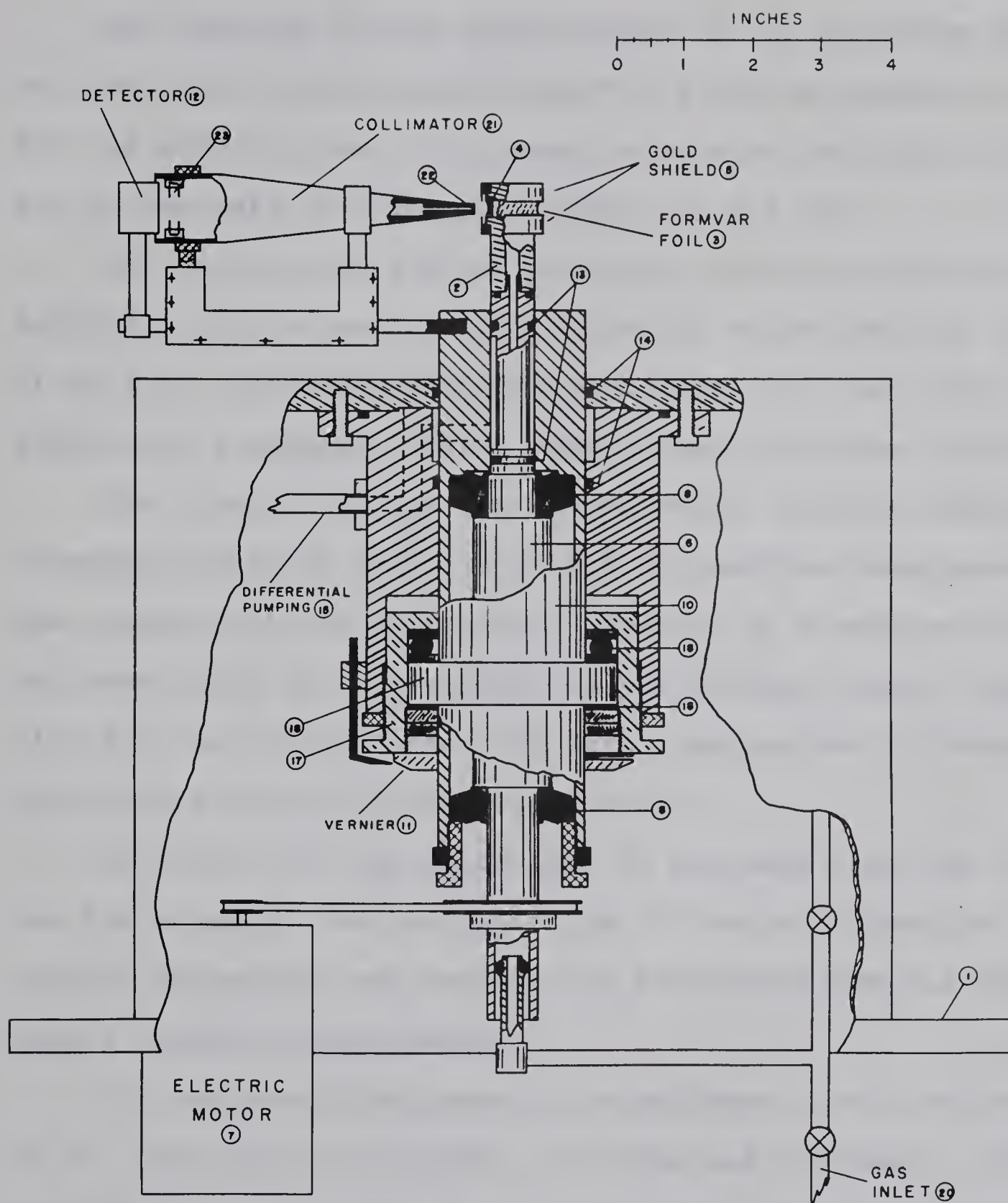


FIG.3-1: GAS TARGET

The function of the center shaft (6) is to rotate the target cell via the variable speed motor* (7) and to provide a path for the entering gas. For smooth operation the shaft is mounted on two sets of tapered bearings (8) and (9).

The function of the second shaft (10) is to position and monitor (via the vernier (11)) the solid state detector (12). It will be noted that two sets of O-rings (13) and (14) and differential pumping (15) are used in sealing these shafts.

The flange (16), on the second shaft, and its associated threaded mechanism (17) allows one to position simultaneously the target cell and solid state detector in a vertical direction and thus align it with respect to the incident beam. Bearing (18) and the teflon washer (19) are incorporated to reduce the operating friction of the second shaft.

As noted, the gas inlet (20) is provided with two channels: one for entering the gas (which is in turn monitored by a mercury monometer) and another for evacuating the gas cell and target chamber simultaneously.

For the associated particle experiment a well defined beam of He^3 particles is required. To this end collimator (21) forms part of the solid state detection system. It is cone shaped with two defining apertures (22) and (23). Its continuous stainless steel structure serves to differentiate against multi-

* Zero-max motor, Model Al-M1; Zero-max, 15 Musgrove St., Toronto 13, Ontario.

ply scattered particles and thus reduces the charged particle background. In addition its cone shape allows one to position the detector to within 5 degrees of the beam. The two apertures, which are easily replaced, subtend an angle of about 4 degrees. This is a reasonable compromise between energy resolution and counting rate. The spacing and size of the collimator apertures form the heart of the geometric problem associated with the efficiency experiment.

The cylindrical gas cell (2) of Fig. 3-1 functioned reasonably well, but was subject to two major weaknesses. Firstly, it was no easy task to produce a completely homogeneous and yet leak tight window over the entire circumference of the gap. And secondly, undue noise was created in the solid state detector when the beam scattered off the tungsten pegs. To overcome these difficulties the alternate design of Fig. 3-2 was used.

It consists of two brass caps (1) and (2) epoxied* to a tantalum cylinder (3), 1" high and 1" in diameter. Along one side of the cylinder is cut a 1/4" wide groove over which is placed a Formvar membrane (4). In addition a 1/4" hole is made in the front and back face of the cylinder. These in turn are covered by sheets of 50 μ in. nickel foil. After passing through a circular collimator, the incident beam enters and exits the

*Plastic Steel, Devcon Corp.

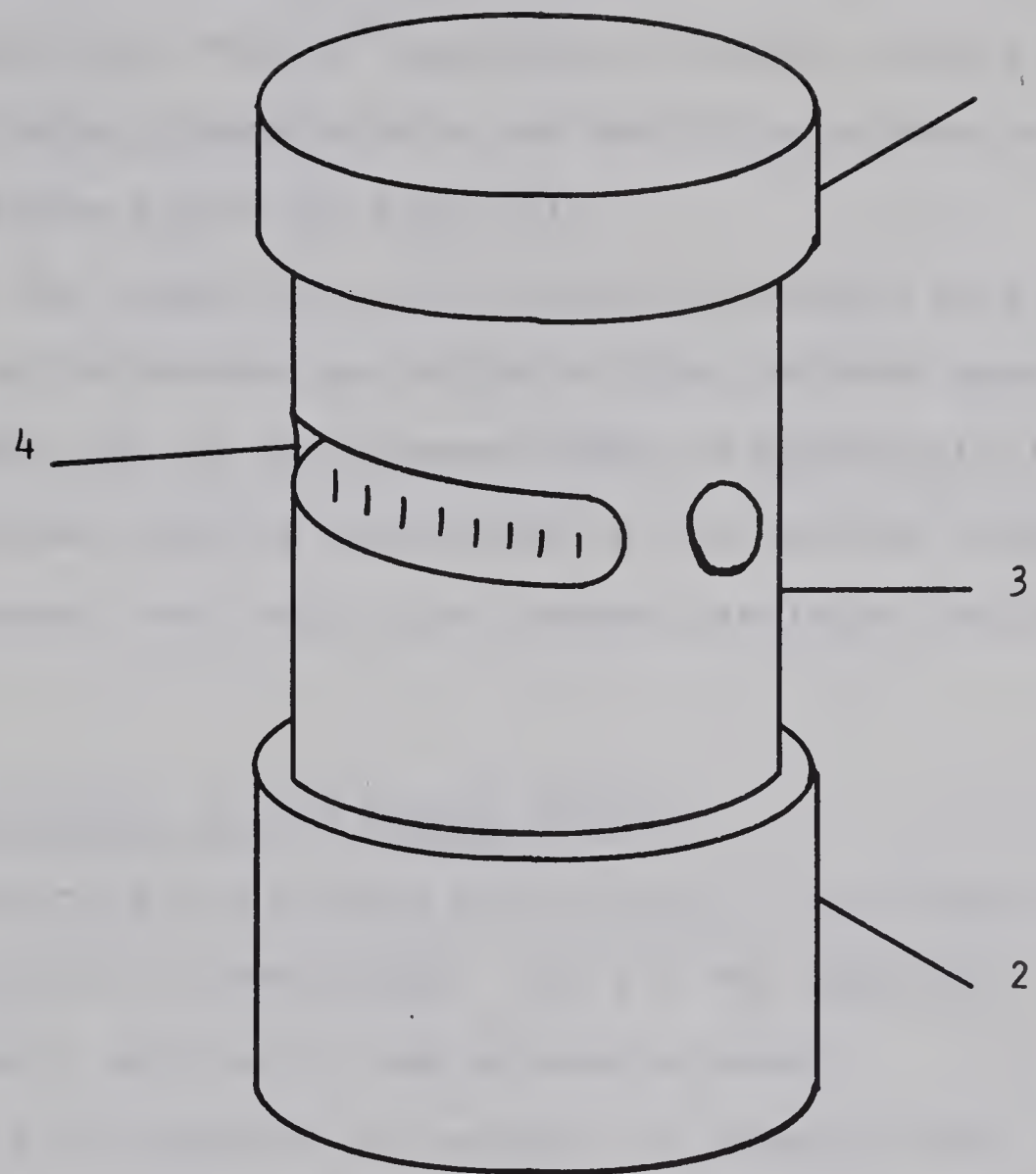


Fig. 3-2: Redesign Of Gas Cell

gas cell through these nickel windows and is in turn stopped by a Faraday cup. The He^3 particles, however, escape through the much thinner Formvar window and are in turn detected by the solid state system of Fig. 3-1.

Since the target does not rotate the Formvar foil is not subjected to the weakening action of the incident beam. In addition the area of the Formvar window is substantially reduced. However, one is restricted in the angular range (30 to 150 degrees) over which the charged particles can be detected.

(iii) Construction of the Formvar Window

In preparing the Formvar foil ($\text{C}_5\text{H}_7\text{O}_2$) a procedure similar to that outlined by Hoogenboom (Ho 61) was adopted. Fig. 3-3 is a schematic outline of the apparatus used.

First a 2% solution (by weight) of Formvar15/95* with ethylene dichloride is prepared. The solution is then dropped, via a burette (20 drops/min.), onto a file partly submerged in a bath of distilled water. (The action of the file being to spread the solution as it enters the bath.) Upon contact with the water a surface tension interaction quickly spreads the solution into a very thin layer, resulting in the rapid evapo-

* Obtained from Shawinigan Resins Corp., Springfield, 5, Mass.

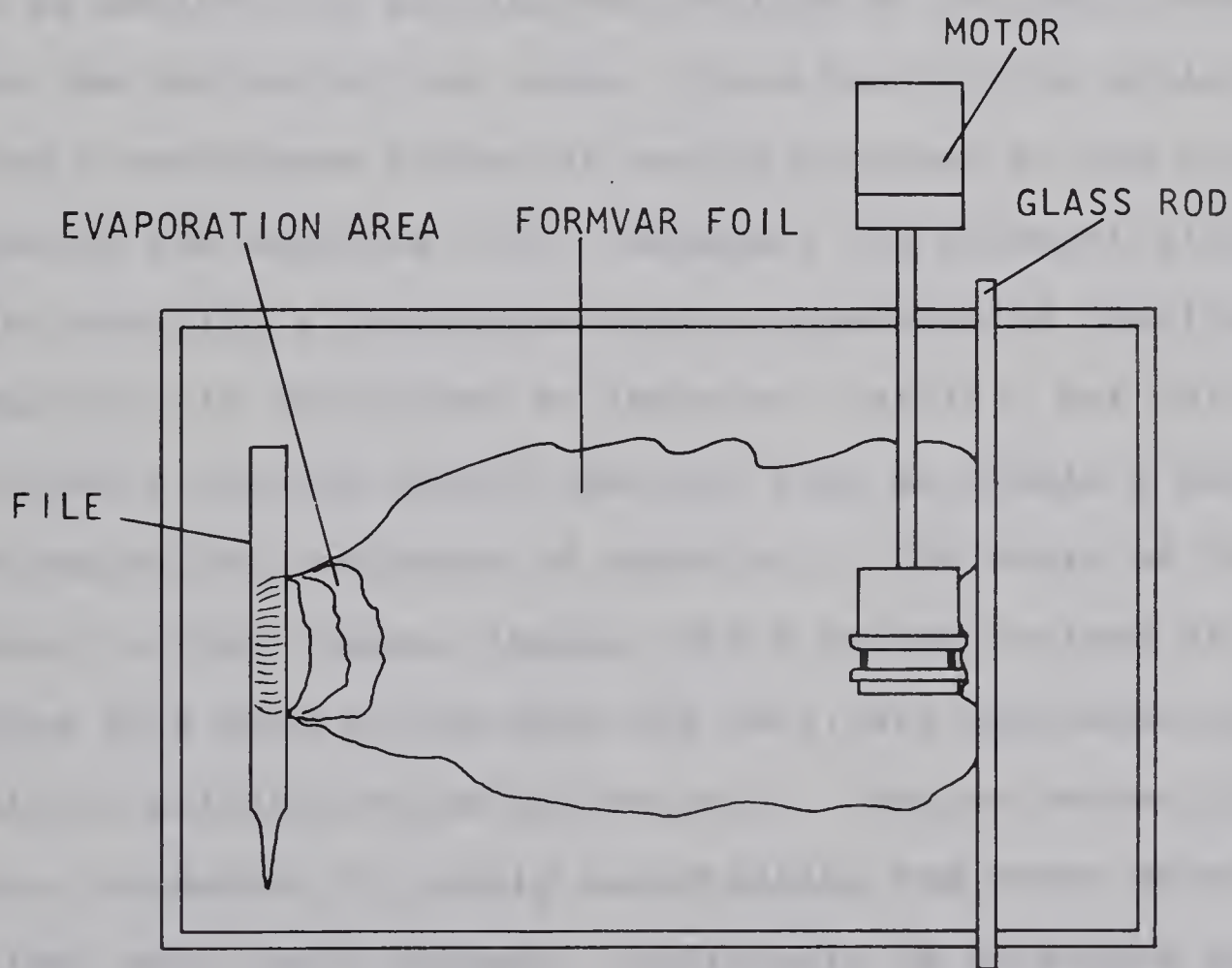
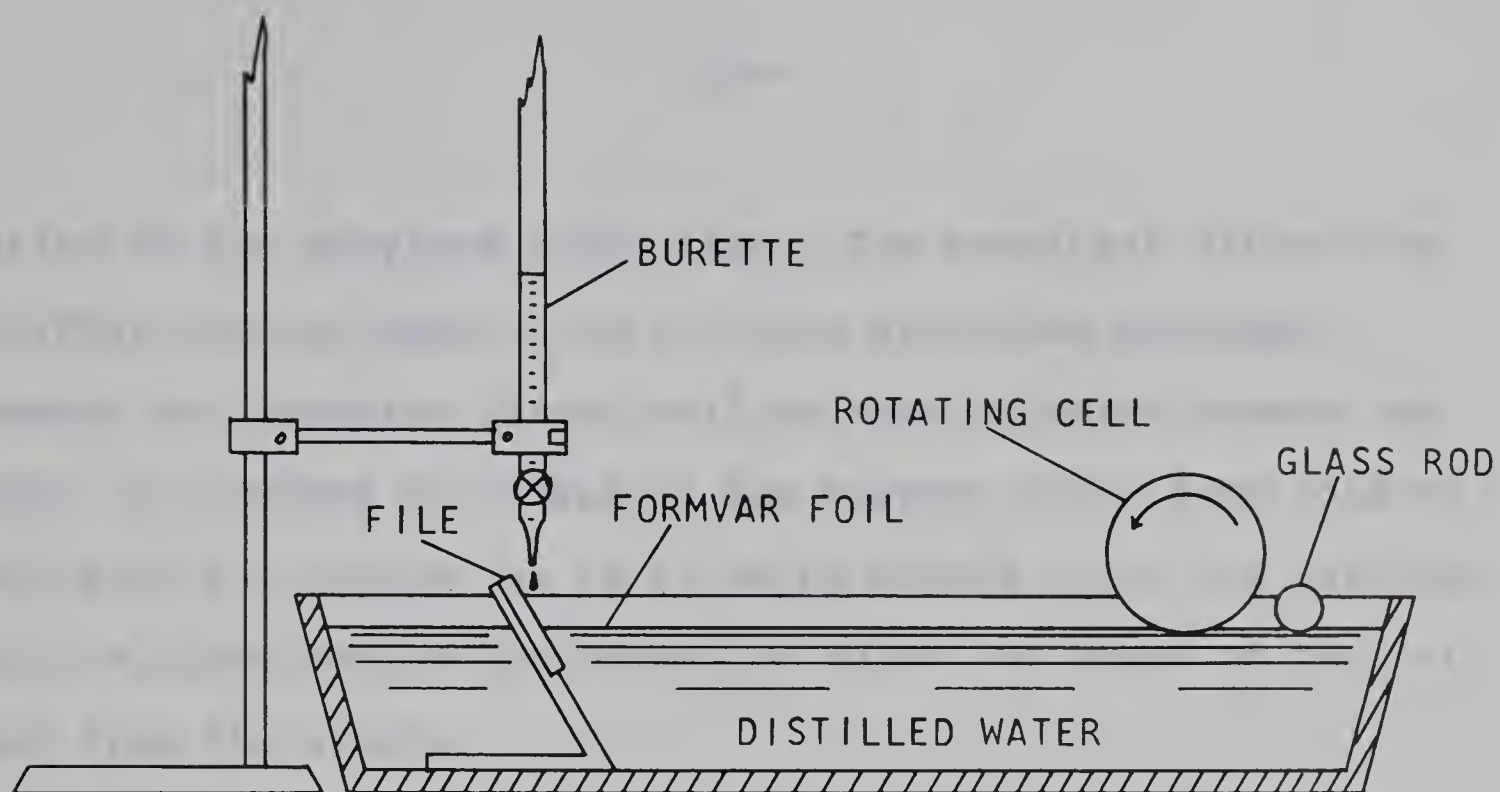


Fig. 3-3: Apparatus For Rolling Foils

ration of the ethylene dichloride. The resultant ultra-thin ($\sim 0.06\mu$) film of about 3 to 4 inches wide then proceeds towards the rotating target cell as more solution enters the bath. To prevent the edges of the Formvar ribbon from folding back over the window, as it is being picked up by the rotating cell, a glass rod is introduced to guide the edges of the foil away from the window.

The initial pickup action of the foil by the rotating cell is achieved by placing the surface of the cell about $1/8$ " below the surface of the water. Once the rolling action begins a continuous ribbon is easily achieved by the pulling action of the rotating cell. However, the greatest difficulty is in obtaining a continuous foil of homogeneous quality. (Homogeneity is considered an important quality, not only to guarantee a uniform energy loss but also to obtain a maximum of strength for a minimum of material.) The basis of the problem is that stress ripples, which become regions of overlapping foil when rolled onto the cell, are generated by the localized pulling action of the cell. One can reduce this action, somewhat, by gently manipulating the outer edges of the foil with one's fingers. Difficulty is sometimes also encountered in getting the foil to spread initially. However, once again, with the gentle manipulation of one's fingers one can encourage the foil towards the rotating cell.

Having obtained the desired number of turns the foil growth is terminated by either removing the source (which results in an additional 3 or 4 much thinner layers from the residual solution on the file) or by placing the glass rod in front of the rotating cell and thereby breaking the foil at the point of contact.

In preparing the target cell for the rolling process consideration had to be given to the sealing properties of the Formvar foil to the gas cell. A number of schemes were tried, but the greatest success was attained by first wetting the contact surface with the 2% Formvar solution, followed immediately by the rolling procedure. In the event of an "abortive roll", ethylene dichloride was used to clean the target cell.

In reality the overall procedure outlined above is far from perfect, but with practice a success rate of 10-20% is obtainable. There is, however, a slight correlation between the success rate and the procedure used in preparing the solution. That is, clear solutions (obtained by allowing the Formvar powder to dissolve slowly in the ethylene dichloride) rather than the milky solutions (resulting from shaking the solution to speed up the dissolving process) seem to be a source of greater success.

Using the procedure outlined above foils ranging in thick-

ness from 30 to 300 keV, with respect to 5.15 MeV Pu^{239}_{α} particles, were constructed. It was found that foils as thin as 50 keV could withstand a pressure gradient of 2 cm. of Hg. and a beam current of 1 μ amp without undue strain.

(iv) Electronics of the Associated Particle Experiment

Fig. 3-4 is a block diagram of the electronic configuration employed by the associated particle experiment. The coincidence imposed by the system allows a neutron to be detected if and only if at the same time a He^3 particle is detected, whereas, all He^3 particles are detected independent of the neutrons.

The neutrons are spectrum analyzed by the usual time-of-flight technique, whereas, the charged particles are spectrum analyzed by a direct pulse height evaluation of the signals coming from the solid state detector. The neutron detector is the same liquid scintillator, Philips XP 1040 phototube combination discussed in Section 2.3. The charged particle detector is a Nuclear Diode PL-2-35-10 surface barrier silicon detector with a 170 μ depletion depth.

The experiment is run with a D.C., rather than pulsed, beam of incident deuterons. The start pulse for the time-to-amplitude converter (T.A.C.) comes from the Ortec time-pickoff unit which is connected in series between the solid state detector and preamplifier. The signal coming from the detector passes through

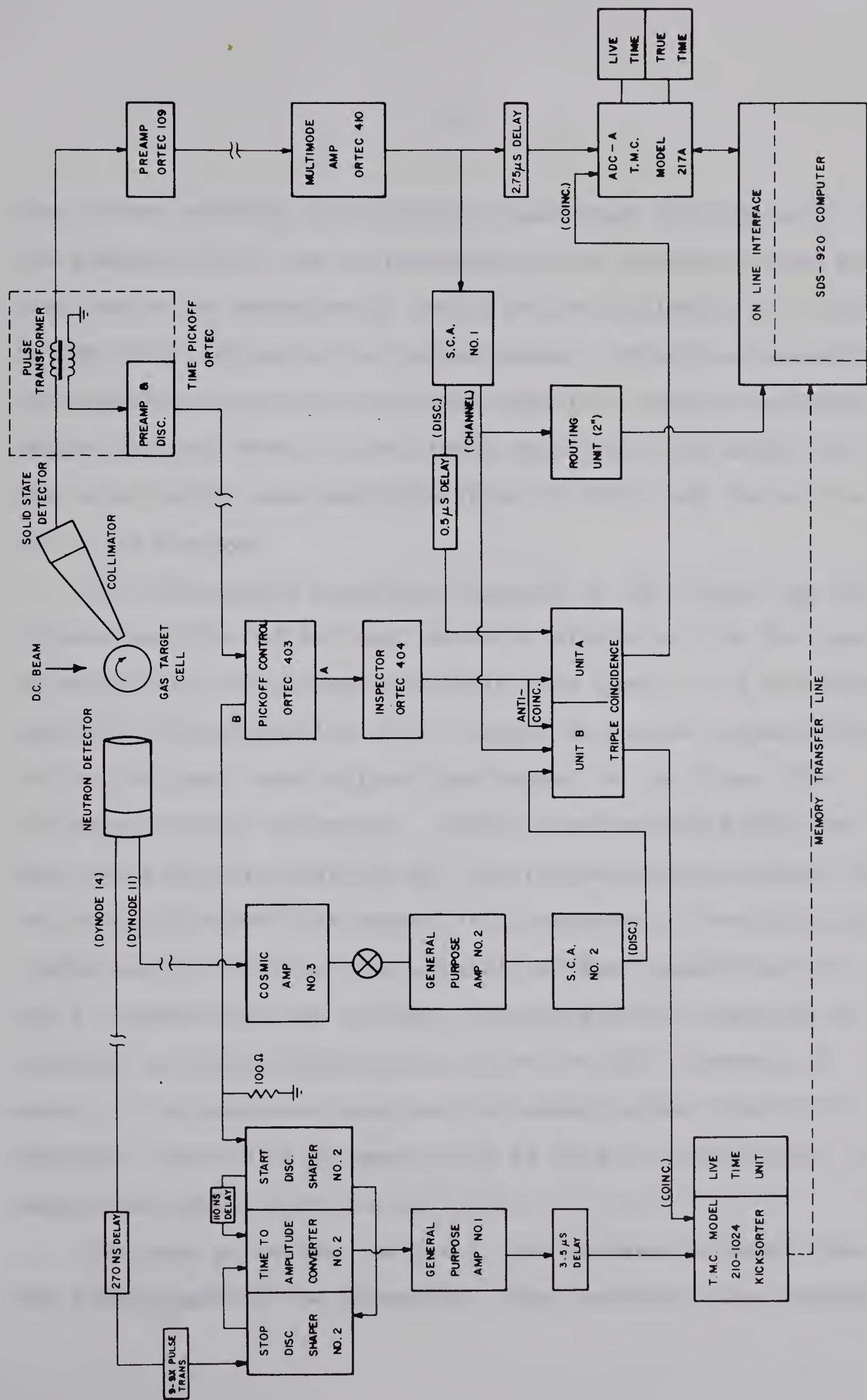


Fig 3-4 Associated Particle Electronics

the primary winding of the pulse transformer and then onto the preamplifier. The corresponding pulse induced in the secondary, which is subsequently amplified and subjected to a discrimination bias, serves as the timing signal. From the preamplifier the original signal is once again amplified and appropriately shaped (by the Ortec 410 Multimode Amplifier) for entry into the pulse height analyzer consisting of ADC-A and the on line SDS - 920 computer.

The coincidence conditions imposed by the window and discrimination bias of S.C.A #1 serve to single out the He^3 peak and to establish a low energy discrimination level. All the pulses above the discrimination level, except for those corresponding to the He^3 peak, are analyzed and stored in the first 1024 channels (0-1023) of memory. Those corresponding to the He^3 peak are similarly analyzed but are routed into the second 1024 channels (1024-2047) of memory (for purposes of identifying the window width). Having once accumulated the respective data for a complete run the original charged particle spectrum is restored by adding together the first two 1024 channels of memory. The resultant spectrum is stored in the third 1024 channels (2048-3071) of memory and is used in establishing the background count under the He^3 peak.

The stop pulse for the T.A.C., as before, is taken from the 14th dynode of the phototube. The resultant time converted

signals are subsequently amplified by G.P.A. #1 and then spectrum analysed and stored by the T.M.C. 210-1024 pulse height analyzer.

The coincidence conditions imposed on the neutron spectrum, as established by Triple Coincidence Unit-B, are:

- (i) that a signal fall within the window setting of S.C.A. #1 (corresponding to the detection of a He^3 particle), and
- (ii) that the photo-election signal, taken from the 11th dynode of the phototube, be above the discrimination level established by S.C.A. #2.

The resultant neutron spectrum is then a single peak corresponding to those neutrons produced in coincidence with a kinematically associated He^3 particle.

At the end of data collection the neutron spectrum stored within the T.M.C. 210-1024 unit is transferred into the fourth 1024 channel memory block of the SDS-920 computer. Fig. 3-5 shows the essential features of the spectral contents of memory. From the computer memory the data is transferred to magnetic tape for further analysis.

It is important to the correct evaluation of the detector efficiency to have the photo-electron threshold level of S.C.A. #2 equal to that used by the spectrometer configuration of Section 2.3. This criterion is fulfilled by maintaining a fixed setting for a parameter whose measurement is sensitive to

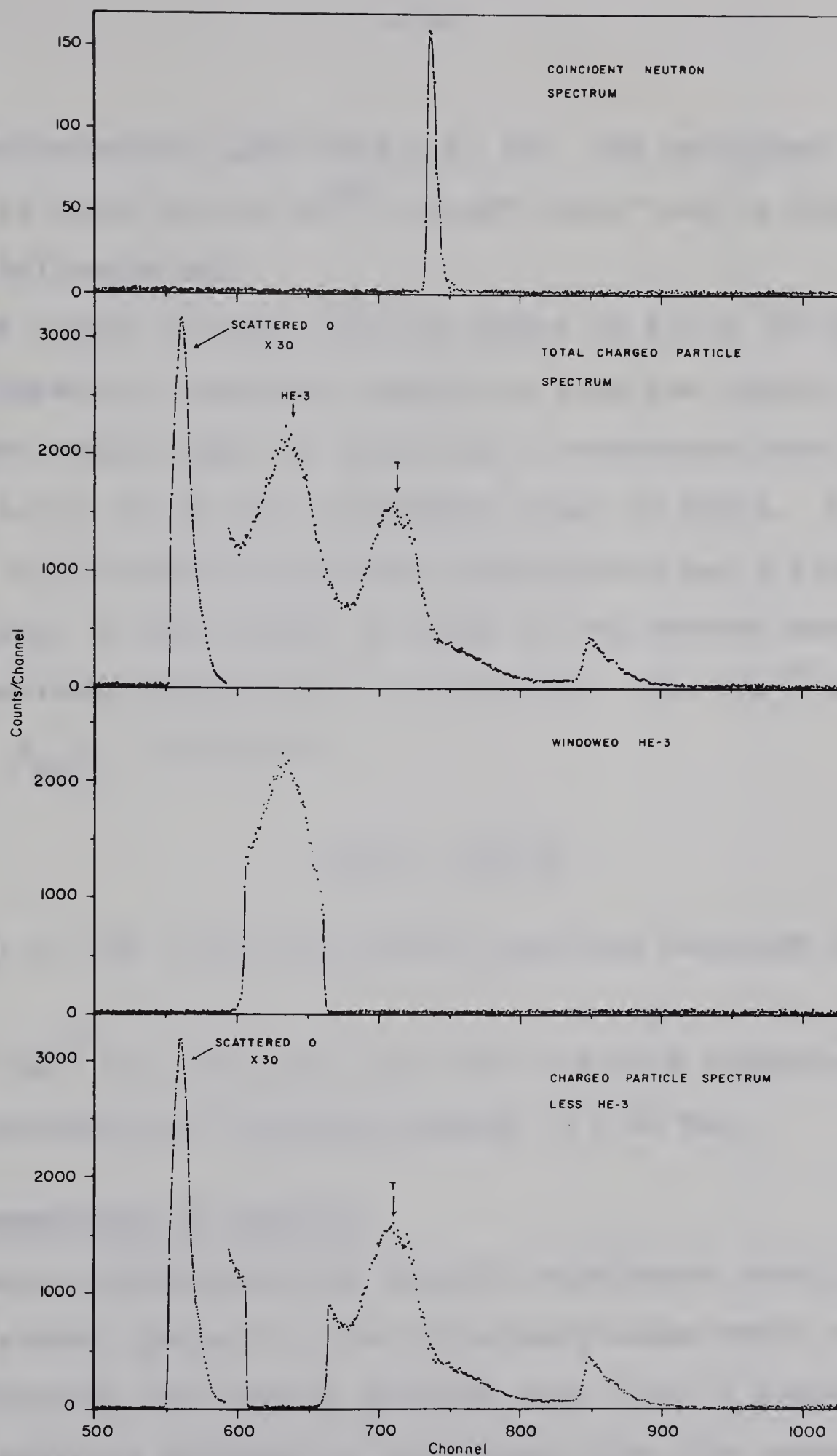


Fig. 3-5: Associated Particle Spectrum

the discrimination level of S.C.A. #2. The parameter so chosen is known as the " Na^{22} cut off ratio" and is determined in the following way.

The inputs of ADC-A and the output of S.C.A. #2 are removed and replaced by a parallel connection from the output of G.P.A. #2 to the analog input of ADC-A and a connection from the output of S.C.A. #2 to the coincidence input of ADC-A. A Na^{22} γ source (0.511 MeV from positron annihilation and 1.274 MeV from Ne^{22} decay) is then placed in front of the neutron detector and the associated pulse height is collected. The " Na^{22} cut off ratio", $R_{\text{Na}22}$, is given by

$$R_{\text{Na}22} = \frac{c - b}{b - a}, \quad (3.2-1)$$

where a, b, and c are the channel positions outlined in Fig. 3-6.

A " Na^{22} cut off ratio" of 3.249 was used throughout, giving a neutron-detection threshold energy of 0.80 MeV.

3.3 Presentation of Results

Having established the desired coincidence conditions a simple minded approach to the efficiency measurement consists of positioning the neutron detector such that it subtends all of the neutrons produced in coincidence with the associated cone of He^3 particles. The absolute efficiency is given by the

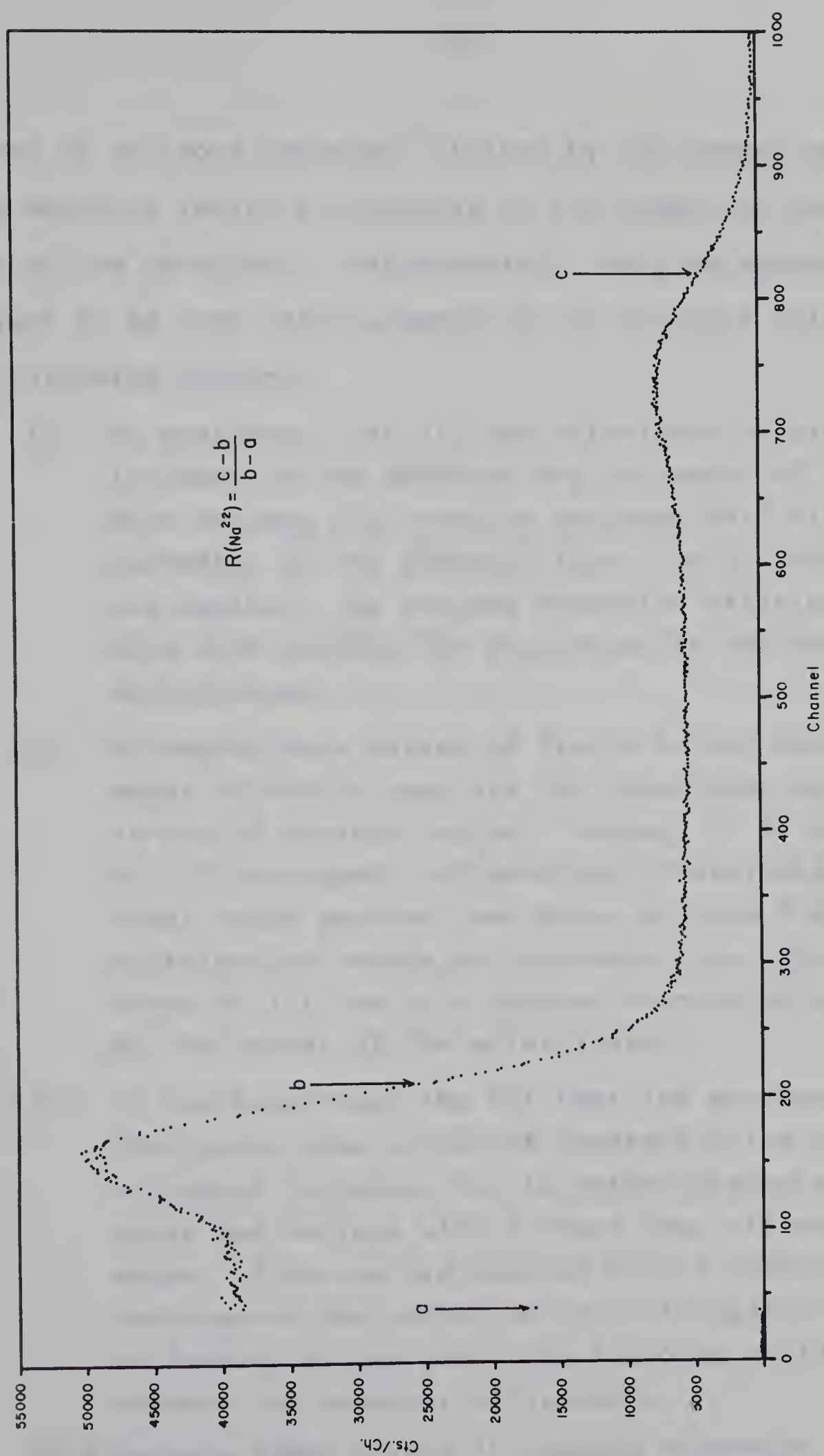


Fig. 3-6: Na^{22} γ -Ray Spectrum

number of neutrons detected, divided by the number of He^3 particles detected (which corresponds to the number of neutrons incident on the detector). Unfortunately, such an approach is subject to an over establishment of the detector efficiency for the following reasons.

- (i) To guarantee that all the coincident neutrons are incident on the detector the perimeter of the coincident neutron flux must be enclosed well within the perimeter of the detector face. As a consequence one neglects the reduced detection efficiency associated with neutron out scattering at the edge of the scintillator.
- (ii) By employing a target of finite volume and a collimator of double aperture the coincident neutron flux is not of constant value. Rather, it is in the form of a flat-topped, 2-dimensional distribution of elliptical cross section (see Figs. A-3 and A-4). Such a distribution serves to complement the edge effect error of (i) due to a further concentration of neutrons at the center of the scintillator.
- (iii) It has been found (Mc 67) that the response of the XP 1040 photo tube is not of constant value with respect to radial distance, but is rather characterized by peaks and valleys with a sharp drop off near the edges. Since we are dealing with a concentration of neutrons at the center of the scintillator, the non-uniformity of the phototube response would tend to enhance the detector efficiency.

To eliminate these errors it becomes necessary to lengthen

the neutron flight path so that the detector face is enclosed within the flat-topped portion of the neutron distribution. In addition to having to contend with a reduced counting rate, it then becomes necessary to evaluate a correction factor, R, giving the fraction of the distribution subtended by the detector. The absolute efficiency is then given by

$$\text{Eff.} = \frac{1}{R} \frac{\text{No. of neutrons detected}}{\text{No. of He}^3 \text{ particles detected}} \quad (3.3 - 1)$$

For the results discussed here the parameter, R, was calculated via a computer program; written by J. F. Easton and discussed under Appendix A.

Fig. 3-7 gives the results of the relative efficiency measurement normalized to an absolute value of 12.8% ($\pm 7\%$) at 2.82 meV. The target geometry, flight path, and R value relative to this measurement are given on the data sheet, Fig. A-2. The corresponding neutron and charged particle spectra are those of Fig. 3-5.

In addition to the experimental data, Fig. 3-7 gives the results of computer generated, theoretical calculations (Gr 67). The model used accounts for multiple neutron scattering within the scintillator plus the influence of neutron-carbon scattering. Due to the rather questionable agreement the experimental curve was used throughout in the analysis of the angular distribution data.

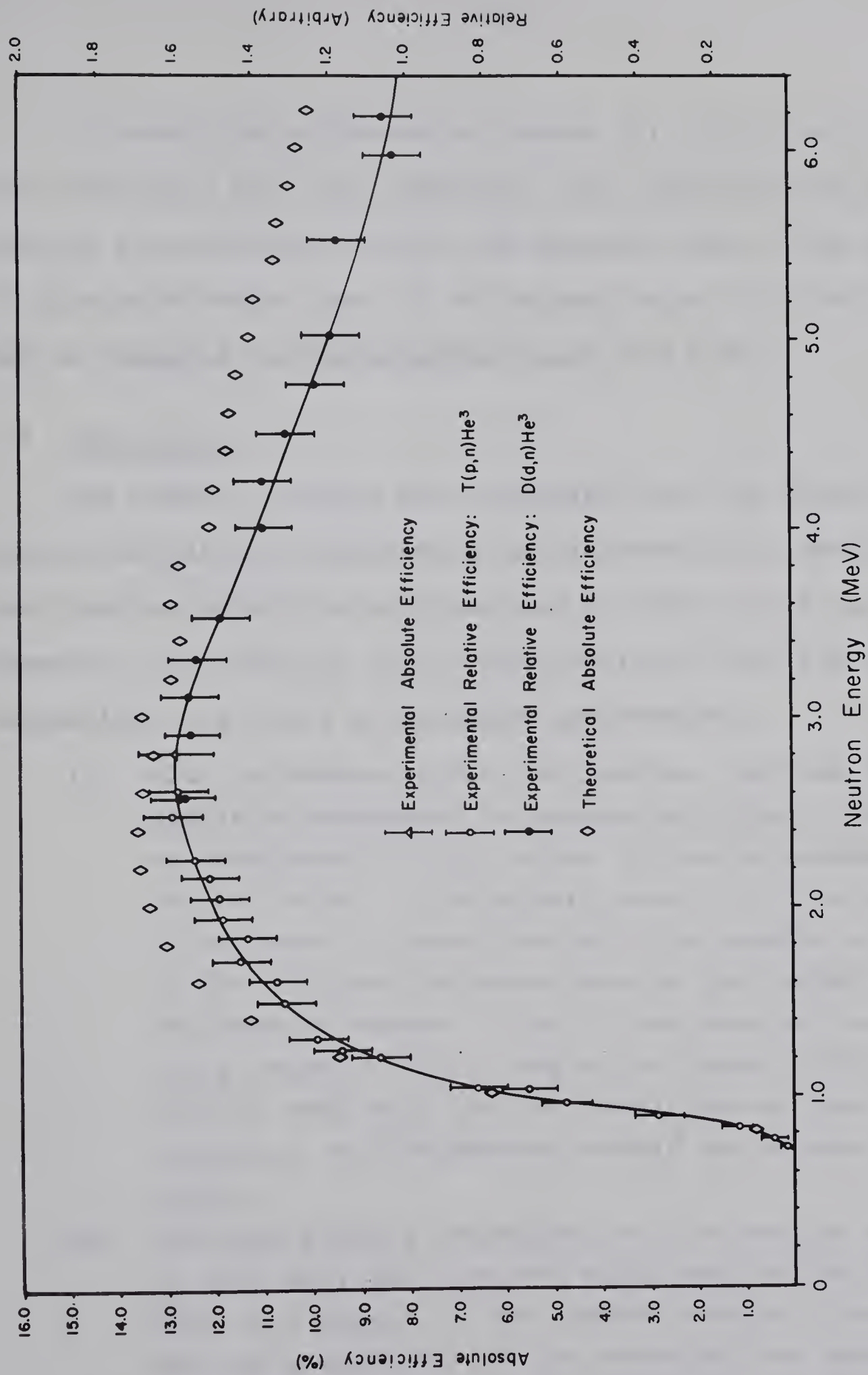


Fig. 3-7: Neutron Detector Efficiency Response

To check the influence of points (i), (ii), and (iii) the associated particle experiment was repeated with the neutron flux enclosed within the detector face. The results of this measurement gave an efficiency value of 18.6% at 2.82 MeV as compared to the accepted value of 12.8%.

3.4 Conclusions

The results of this work indicate that the ideas of an associated particle experiment are successful in obtaining absolute neutron detection efficiencies to within an accuracy of 7%. However, the technique is far from perfected and the following suggestions are given as possible improvements.

- (i) With reference to Fig. 3-5 we see that the charged particle background is excessively high, leading to an unnecessarily high error in the determination of the He^3 count. The primary source of this background is believed to come from multiple elastic scattering of the incident deuteron beam by the target and collimation system. Thus if one were to use a solid state detector with a depletion layer sufficiently thin to stop only the He^3 particles and not the deuterons, the background should be reduced significantly.
- (ii) The most glaring inadequacy of the results of Fig. 3-7 is that only one absolute efficiency point is given. This is a result of the limited running time allowed for the experiment and the restrictions imposed on angle and energy for which the He^3 peak was reasonably

isolated. The basis of this problem was a small concentration of oxygen in the deuterium gas. The resultant deuteron-oxygen elastic scattering produced a peak near the He^3 and tritium peaks and equal in magnitude. It was only through a judicious choice of angles that the He^3 peak could be separated from the scattered D-D peak on the one hand and the scattered D-Oxygen peak on the other. For the angle chosen (31.2°) the two scattered peaks merged, leaving the He^3 and tritium peaks reasonably well isolated. To overcome this problem a purer supply of deuterium is suggested.

CHAPTER IV

THE $\text{Ne}^{20}(\text{d},\text{n})\text{Na}^{21}$ REACTION

4.1 Introduction

The study of the $\text{Ne}^{20}(\text{d},\text{n})\text{Na}^{21}$ reaction at $E_d = 3.924$ MeV was undertaken with the following objectives in mind;

- (i) to initiate a search for new low lying levels in the Na^{21} nucleus;
- (ii) to obtain spectroscopic information about the Na^{21} nucleus from a D. W. B. A. analysis of absolute cross section data; and
- (iii) to corroborate the experimental results within the framework of the collective model.

The established structure of Na^{21} , and its minor nucleus Ne^{21} , is illustrated in Fig. 4-1. The $3/2^+$ assignment, for the Na^{21} ground state, has been established by the superallowed character of its β^+ decay to the ground state of Ne^{20} (En 62) and also by an atomic-beam, magnetic resonance experiment (Am 65). The early results of $\text{Ne}^{20}(\text{d},\text{n})\text{Na}^{21}$ stripping experiments restricted the J^π value of the Na^{21} 0.335 level to either $3/2^+$ or $5/2^+$. C. Van der Leun and W. L. Monton (Va 64) singled out the $5/2^+$ value, via a $\text{Ne}^{20}(\text{p},\gamma)\text{Na}^{21}$ experiment.

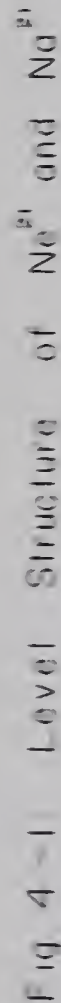


Fig. 4-1 Level Structure of Ne^{21} and Nd^{21}

The $7/2^+$ value for the Na^{21} 1.751 level has been assigned on the basis of mirror-pair arguments and a $\text{Ne}^{20}(\text{p},\gamma)\text{Na}^{21}$ correlation experiment (Al 65). The Na^{21} 2.433 level has been readily identified from $\text{Ne}^{20}(\text{d},\text{n})\text{Na}^{21}$ stripping experiments as a $\ell\text{p}=0$ transfer, and thus the $1/2^+$ assignment.

The question of additional low lying structure for the Na^{21} nucleus has been suggested by the following work.

(i) J. B. Marion (Ma 56), in a $\text{Ne}^{20}(\text{d},\text{n})\text{Na}^{21}$ threshold experiment, claims to have measured a level at 1.46 ± 0.04 MeV. He does not claim, however, to have measured the 1.75 MeV. level established by subsequent $\text{Ne}^{20}(\text{d},\text{n})\text{Na}^{21}$ work (Aj 61 and Be 61). R. E. Benenson (Be 61), in addition to studying the $\text{Ne}^{20}(\text{d},\text{n})\text{Na}^{21}$ reaction, also studied the $\text{Ne}^{20}(\text{p},\gamma)\text{Na}^{21}$ reaction and claims to have measured a 1.42 ± 0.04 MeV. γ -ray. As its possible source he suggests either a ground state decay from the questionable 1.46 level or an element of a triple cascade from the 1.75 MeV. level to the 0.33 MeV. level after having been fed from the 3.56 MeV. level. Although the evidence is not overwhelming, he suggests the latter as the more acceptable scheme. This same conclusion is reached by Arnell and Sterner (Ar 63) after repeating the $\text{Ne}^{20}(\text{p},\gamma)\text{Na}^{21}$ experiment. The arguments are not conclusive, however, and could be disregarded if subsequent evidence for a Na^{21} 1.46 MeV. level was found.

(ii) W. R. Gibbs (Gi 65) in a study of the $\text{Ne}^{20}(\text{d},\text{n}\gamma)\text{Na}^{21}$

reaction suggests the slight possibility that either the ground or first excited state of Na^{21} might be a double state.

(iii) F. Everling (Ev 63) in a study of the total nuclear binding of excited states for the 2s - 1d subshells suggests the possibility of a $1/2^+$ level at 2.18 MeV. in Na^{21} .

(iv) Recently it has been shown (Po 67 and Ho 67) that the Ne^{21} 2.80 MeV. level is in reality a 2.797 and 2.790 MeV. doublet. This evidence then supports possible doublet structure for the 2.433 MeV. level of Na^{21} , since it is the mirror-pair analog of the Ne^{20} 2.80 level.

Since the energy resolution capability of the neutron spectrometer used at this laboratory is significantly superior to that obtained in any previous $\text{Ne}^{20}(\text{d},\text{n})\text{Na}^{21}$ work, it was felt that further study of this reaction might unearth possible doublet structure. The choice of reaction energy ($E_d=3.924$ MeV.) capitalized on the increased resolution associated with lower energies and yet allowed for the study of all the bound states of Na^{21} .

In addition to a search for new low lying structure, the present experiment served to provide additional absolute cross section data to add to the limited amount reported to date (Aj 61) and (Pe 65). And with the aid of a Distorted Wave Born Approximation (D. W. B. A.) program, written by B. E. F. Macefield (Ma 64), spin and parity assignments were checked and absolute spectroscopic factors obtained.

To complete the treatment of the $\text{Ne}^{20}(\text{d},\text{n})\text{Na}^{21}$ experiment, a discussion of the structure of Na^{21} is made within the framework of the collective model. In this context the absolute spectroscopic factors are interpreted in terms of the expansion coefficients of the Nilsson model wave functions.

4.2 The Experiment

The $\text{Ne}^{20}(\text{d},\text{n})\text{Na}^{21}$ experiment, at a reaction energy of 3.924 ± 0.01 MeV., was performed using the time-of-flight system and gas target cell described in Chapter II. The average deuteron beam current ranged from 1.25 to 2.00 $\mu\text{amps.}$ at an energy of 4.004 ± 0.006 MeV. (An energy loss of 80 KeV. could then be attributed to the 50 μin nickel foil and neon gas.)

The Ne^{20} target consisted of the gas cell (Fig. 2-3) filled to a pressure of about 43 cm. of Hg. (at 27°C) with 99.9 molar % Ne^{20*}). This corresponded to a target thickness of about 290 $\mu\text{gm}/\text{cm}^2$.

The neutrons were timed over a flight path of 6.05 meters at 19 different angles ranging from zero to 140 degrees. For each angle a charge of 1500 $\mu\text{coul.}$ was collected. A timing resolution of 0.96 ns. for the 4.01 MeV. zero-degree, ground-state neutrons was obtained.

The monitor detector was positioned at -20° with respect to the incident beam and at a distance of 3 meters from the

* Obtained from Monsanto Research Corp., Mound Laboratory, Miamisburg, Ohio, U. S. A.

target. Due to its strength and isolation, the Na^{21} 2.433 MeV. monitor peak area was used as the angular distribution normalization factor.

A calibration of the kicksorter was achieved by running the $\text{Be}^9(\text{d},\text{n})\text{B}^{10}$ reaction, at 3.00 MeV, immediately following the $\text{Ne}^{20}(\text{d},\text{n})\text{Na}^{21}$ experiment. The flight times for the respective levels of B^{10} were calculated by a relativistic kinematic program (Gr 67a) on the basis of the measured neutron flight path (6.05 M.) and the known level structure of B^{10} (Aj 66). The corresponding peak positions were then least squares fitted, by a general least squares fitting program (Da 66), to a quadractic equation relating channel position to flight time.

The $\text{Ne}^{20}(\text{d},\text{n})\text{Na}^{21}$ reaction energy of $3.924^{+0.01}$ MeV. was determined by first using the calibration equation to obtain the flight time corresponding to the ground state peak of the run taken at 20 degrees. A variation in the reaction energy required by the kinematic program was then made until the kinematically generated flight time was equal to that determined by the calibration equation. The ground state was used in this determination since, of the levels excited, its Q value is known to the highest degree of accuracy ($0.208^{+0.008}$ MeV. (La 66)).

Fig. 4-2 is the neutron spectrum corresponding to a detection angle of 20 degrees, and is characteristic of the spectra obtained. The contaminate levels due to oxygen and carbon are believed to come from either the nickel foil or tantalum backing used in the construction of the gas cell. It should be pointed

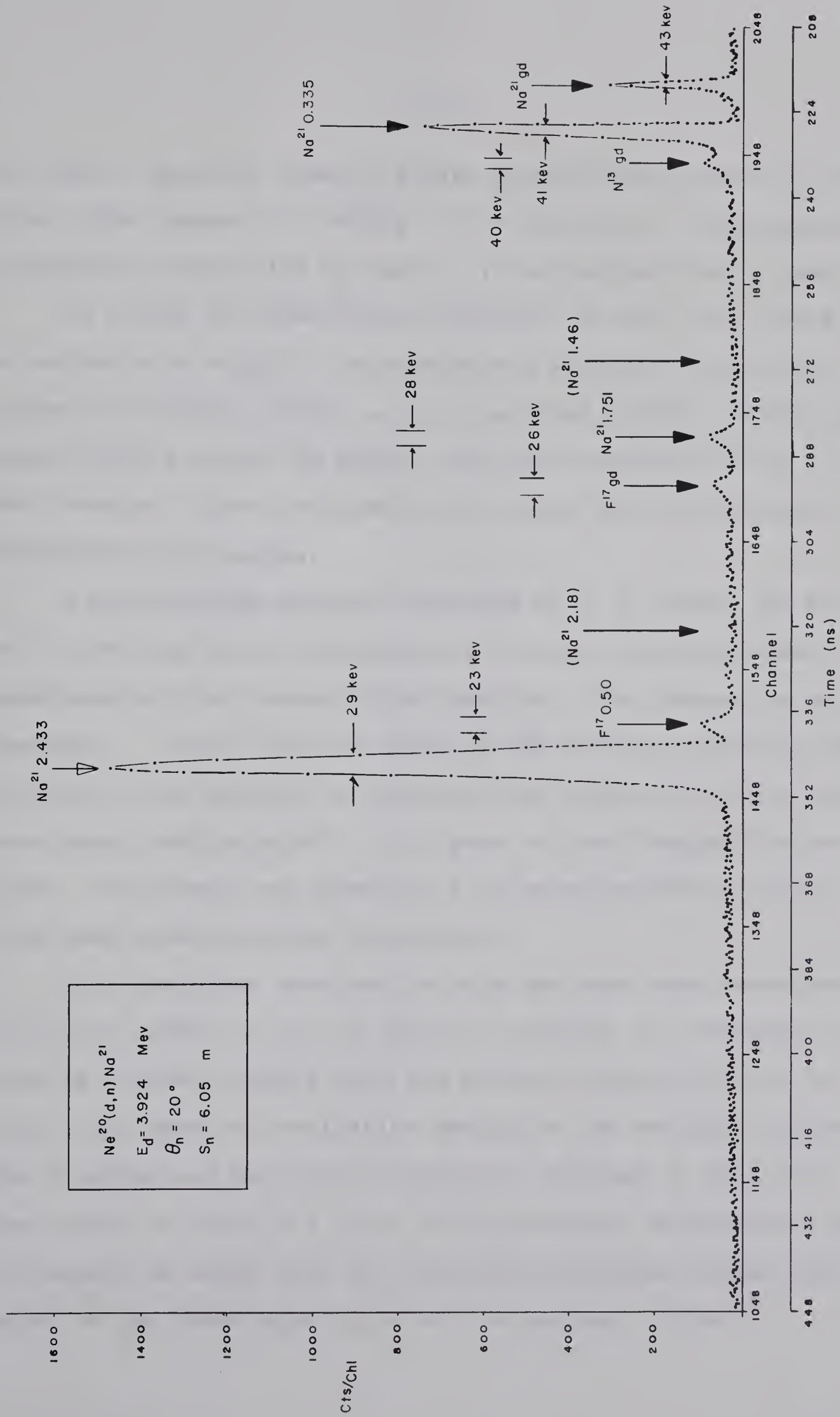


Fig. 4 - 2: Neutron Time Spectrum

out that a parallel time-of-flight spectrum was formed in the first 1024 channels of memory. It consisted of those signals incorrectly identified by the $n - \gamma$ discriminator as γ -rays.

To within the resolution indicated by Fig. 4-2, there is no evidence to support the existence of doublet structure in either the ground, first, or third excited states. In addition there is no evidence to support the questionable 1.42 or 2.18 MeV. levels. These conclusions are borne out by the spectra obtained at all angles.

A peak fitting program developed by J. W. Tepel (Te 66 and Gr 66) was used in determining the peak areas and peak positions of the time-of-flight spectra. The program is so designed such that the shape of the analytic function used in the fitting process is determined by a characteristic reference peak. For this the Na^{21} 2.433 peak of the 5 degree run was used. Consistent and objective fits were obtained by using this same reference peak throughout.

Peak positions obtained in this way were then converted to flight times via the calibration equation and subsequently used by a least squares mass and Q-value program (Da 66) to obtain the mass and excitation energy of the residual nucleus. The Q-values and excitation energies, obtained in this way, are listed in Table 4-1 along with previously determined values. (It should be noted that the excitation energies listed are based on the known mass value of the residual nucleus.)

TABLE 4-1

Q Values and Excitation Energies

Nuclear Level	THIS EXPERIMENT		PREVIOUS WORK		
	Q Value (MeV)	Excitation (MeV)	Q Value (MeV)	Excitation (MeV)	Reference
gnd	$0.208^{+0.008}_{-0.008}^*$		$0.230^{+0.03}_{-0.03}$		Aj 61
			$0.220^{+0.03}_{-0.03}$		Be 61
1st	$-0.127^{+0.01}_{-0.01}$	$0.335^{+0.01}_{-0.01}$	$-0.140^{+0.04}_{-0.04}$	$0.370^{+0.04}_{-0.04}$	Aj 61
			$-0.080^{+0.03}_{-0.03}$	$0.330^{+0.03}_{-0.03}$	Be 61
				$0.338^{+0.003}_{-0.003}$	Va 64
				$0.342^{+0.008}_{-0.008}$	Gi 65
2nd	$-1.543^{+0.015}_{-0.015}$	$1.751^{+0.015}_{-0.015}$	$-1.460^{+0.04}_{-0.04}$	$1.730^{+0.04}_{-0.04}$	Aj 61
			$-1.550^{+0.05}_{-0.05}$	$1.770^{+0.04}_{-0.04}$	Be 61
3rd	$-2.225^{+0.01}_{-0.01}$	$2.433^{+0.01}_{-0.01}$	$-2.201^{+2.007}_{-2.007}$	$2.431^{+0.031}_{-0.031}$	Aj 61
			$-2.200^{+0.04}_{-0.04}$	$2.420^{+0.04}_{-0.04}$	Be 61

*This value was not determined in this experiment but is that given by (La 66). All excitation energies listed are based on this ground state Q value.

Absolute cross section, angular distribution data was obtained for the $\text{Ne}^{20}(\text{d},\text{n})\text{Na}^{21}$ reaction by subjecting the peak fitted results to the following corrections:

- (i) the neutrons incorrectly identified as γ -rays were added to their neutron spectrum counterparts;
- (ii) the resultant sum was divided by the area of the Na^{21} 2.433 monitor peak. (This corrected for any variation in target thickness, charge collection, or run time.);
- (iii) a correction due to the difference in live times between the main and monitor systems was made;
- (iv) a correction due to a variation in detection efficiency was made;
- (v) and finally, the resultant relative angular distributions were normalized to an absolute determination made at 20 degrees.

Tables 4-2 to 4-5 list the results of this work.

Most reactions designated as "direct" have a small component of compound reaction formation present. This compound reaction component is energy dependent as identified by strong resonant structure, in the absorption cross section, around energies corresponding to the population of excited states in the compound nucleus. As the absorption cross section goes up the cross section in the exit channels also goes up. Thus by

TABLE 4-2

$\text{Ne}^{20}(\text{d},\text{n})\text{Na}^{21}$ Ground State

$\theta(\text{Lab})$ Deg	$\frac{d\sigma}{d\Omega} \frac{\text{mb}}{\text{St}}$ (Lab)	$\theta(\text{c.m.})$ Deg	$\frac{d\sigma}{d\Omega} \frac{\text{mb}}{\text{St}}$ (c.m.)	$\frac{d\sigma}{d\Omega}$ % error
0.27	1.43	0.29	1.25	10.0
5.03	-	5.37	-	-
10.28	1.38	10.97	1.21	8.2
15.11	1.27	16.24	1.12	9.4
20.73	1.15	22.11	1.02	8.5
25.82	1.07	27.51	0.951	8.2
30.20	0.919	32.16	0.820	9.5
36.02	0.895	38.31	0.805	9.0
41.20	0.833	43.76	0.755	9.5
45.40	0.767	48.17	0.700	10.1
51.27	0.635	54.30	0.585	10.4
60.75	0.545	64.14	0.511	12.8
71.45	0.521	75.14	0.500	13.1
75.65	0.524	79.42	0.508	12.6
90.55	0.564	94.44	0.566	11.0
100.43	0.628	104.26	0.645	9.9
115.45	0.637	118.96	0.677	9.8
120.00	0.699	123.37	0.750	10.0
139.53	0.579	142.05	0.644	10.4

TABLE 4-3

$\text{Ne}^{20}(\text{d}, \text{n})\text{Na}^{21}$

0.335 MeV Level

θ (Lab) Deg	$\frac{d\sigma}{d\Omega}$ (Lab) $\frac{\text{mb}}{\text{St}}$	θ (c.m.) Deg	$\frac{d\sigma}{d\Omega}$ (c.m.) $\frac{\text{mb}}{\text{St}}$	$\frac{d\sigma}{d\Omega}$ % Error
0.27	1.39	0.29	1.21	11.9
5.03	1.44	5.39	1.26	10.3
10.28	1.75	11.01	1.53	10.0
15.22	2.37	16.29	2.03	9.9
20.73	3.60	22.17	3.17	9.4
25.82	4.82	27.59	4.26	8.7
30.20	5.73	32.25	5.09	8.5
36.02	6.36	38.42	5.69	7.9
41.20	6.69	43.88	6.03	7.7
45.40	6.50	48.30	5.90	8.6
51.27	5.99	54.45	5.50	9.1
60.75	4.72	64.30	4.42	9.0
71.45	3.19	75.31	3.06	9.4
75.65	2.43	79.60	2.35	8.3
90.55	1.49	94.62	1.50	9.0
100.43	1.20	104.44	1.23	9.0
115.45	1.11	119.13	1.18	8.9
120.00	1.23	123.53	1.326	9.1
139.53	1.14	142.17	1.27	9.6

TABLE 4-4

$\text{Ne}^{20}(\text{d}, \text{n})\text{Na}^{21}$ 1.751 MeV. Level

$\theta(\text{Lab})$ Deg	$\frac{d\sigma}{d\Omega}(\text{Lab}) \frac{\text{mb}}{\text{St}}$	$\theta(\text{c.m.})$ Deg	$\frac{d\sigma}{d\Omega}(\text{c.m.}) \frac{\text{mb}}{\text{St}}$	$\frac{d\sigma}{d\Omega} \% \text{ Error}$
0.27	0.439	0.30	0.368	12.8
5.03	0.395	5.50	0.331	14.8
10.28	0.454	11.23	0.381	13.8
15.22	0.478	16.61	0.403	11.8
20.73	0.400	22.61	0.339	12.4
25.82	0.496	28.13	0.423	10.3
30.20	0.570	32.87	0.489	11.9
36.02	0.552	39.14	0.478	17.0
41.20	0.557	44.70	0.488	15.0
45.40	0.512	49.18	0.452	13.5
51.27	0.565	55.41	0.506	12.8
60.75	0.392	65.38	0.360	15.1
71.45	0.460	76.48	0.436	17.7
75.65	0.511	80.79	0.490	16.5
90.55	0.560	95.86	0.563	12.8
100.43	0.456	105.65	0.474	13.5
115.45	0.345	120.24	0.376	14.3
120.00	0.366	124.60	0.404	14.4
139.53	0.253	142.97	0.293	22.4

TABLE 4-5

$\text{Ne}^{20}(\text{d},\text{n})\text{Na}^{21}$		2.433 MeV. Level		
θ (Lab) Deg	$\frac{d\sigma}{d\Omega}$ (Lab) $\frac{\text{mb}}{\text{St}}$	(c.m.) Deg	$\frac{d\sigma}{d\Omega}$ (c.m.) $\frac{\text{mb}}{\text{St}}$	$\frac{d\sigma}{d\Omega}$ % Error
0.27	61.85	0.30	49.87	7.1
5.03	57.32	5.60	46.26	7.2
10.28	47.52	11.44	38.45	7.3
15.22	39.04	16.93	31.72	7.2
20.73	25.29	23.04	20.68	7.2
25.82	16.08	28.66	13.25	6.6
30.20	11.29	33.48	9.37	7.3
36.02	6.78	39.85	5.69	8.5
41.20	5.88	45.49	5.01	11.2
45.40	5.92	50.04	5.09	11.8
51.27	7.10	56.36	6.21	9.6
60.75	8.54	66.44	7.70	9.7
71.45	8.26	77.64	7.73	8.2
75.65	7.66	81.97	7.28	7.6
90.55	5.36	97.07	5.40	9.4
100.43	4.11	106.85	4.31	10.5
115.45	2.34	121.38	2.60	8.4
120.00	2.43	125.65	2.75	8.6
139.53	1.65	143.76	1.98	9.5

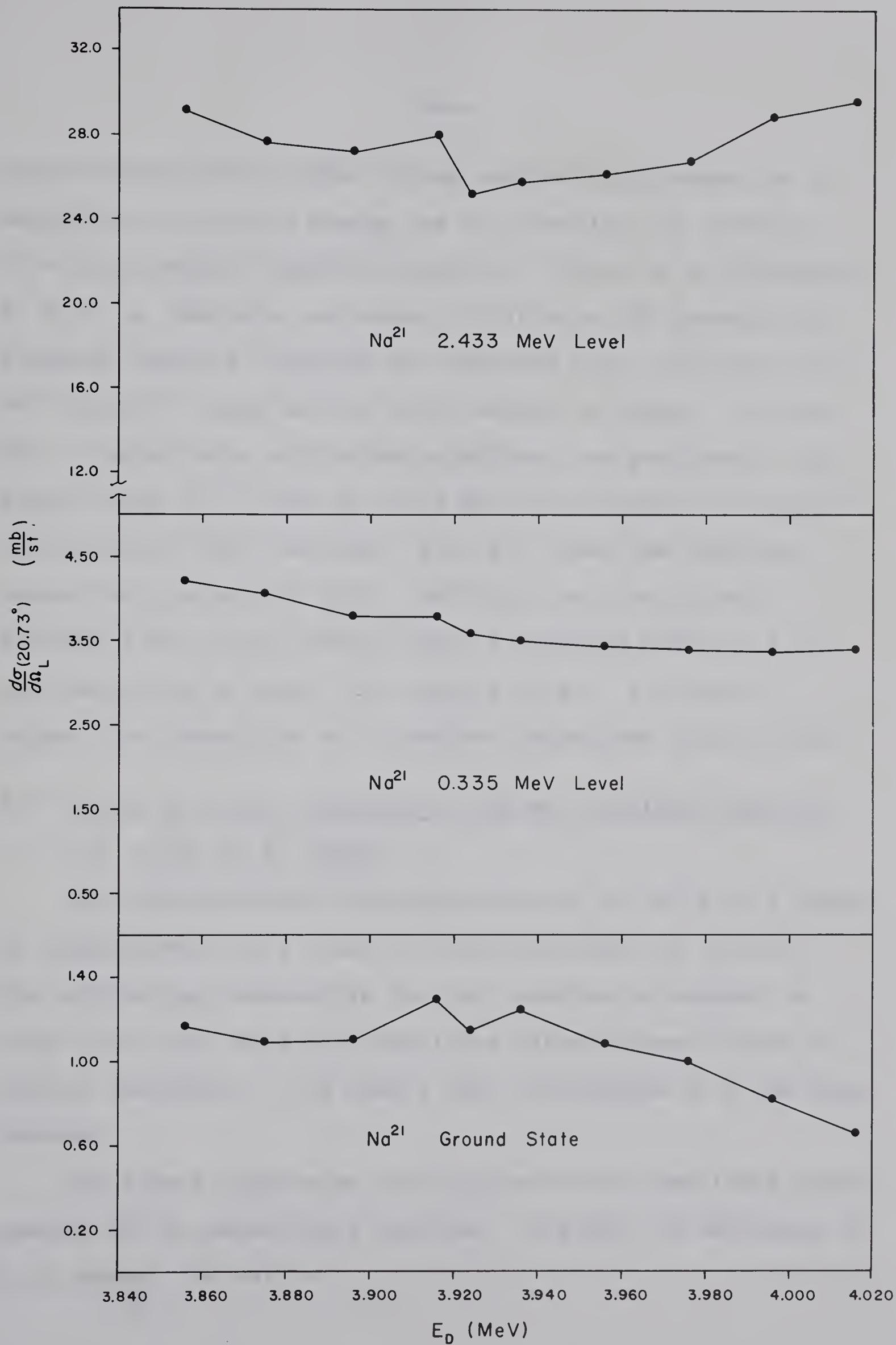


Fig. 4-3: Yield Curves

measuring the $\text{Ne}^{20}(\text{d},\text{n})\text{Na}^{21}$ cross section with respect to a variation in reaction energy one can identify the presence of strong compound reaction formation. Since in an effective D. W. B. A. analysis one wishes to minimize the presence of compound reaction formation one searches for a minimum in the $\text{Ne}^{20}(\text{d},\text{n})\text{Na}^{21}$ cross section with respect to energy. To this end a single angle excitation experiment was performed. The energy range $E_d = 3.856$ to 4.016 MeV. was covered at a detection angle of 20.73 degrees. Fig. 4-3 gives the resultant curves for the ground, first, and third excited states. Although total cross section data is required before a firm conclusion can be drawn, the results of Fig. 4-3 tend to support the assumption of a constant background contribution.

4.3 The D. W. B. A. Analysis of the $\text{Ne}^{20}(\text{d},\text{n})\text{Na}^{21}$ Reaction

(i) D. W. B. A. Theory

The distorted-wave Born-approximation (D. W. B. A.) theory is a description of a class of reactions known as "direct". The interaction responsible for the reaction is assumed to occur just once, with the transition taken between states of elastic scattering. The theory then corresponds to a one step process.

The formal expression for the transition amplitude corresponding to the generalized reaction, $A(a,b)B$, as developed by R. H. Bassel (Ba 64) is:

$$T_{DW} = \int d\vec{r}_a \int d\vec{r}_b \chi_b^{*(-)}(\vec{k}_b, \vec{r}_b) \langle Bb | V | Aa \rangle \chi_a^{(+)}(\vec{k}_a, \vec{r}_a) \quad (4.3-1)$$

Here \vec{r}_a is the displacement of 'a' from 'A' and \vec{r}_b the displacement of 'b' from 'B'. J is the Jacobian of the transformation to these relative coordinates. The functions $\chi_a^{(+)}$ and $\chi_b^{(-)}$ are the elastic scattering states, where (+) and (-) denote the usual outgoing and incoming boundary conditions. V is the interaction potential and $|Aa\rangle$ and $|Bb\rangle$ are the internal states of the colliding pairs before and after the reaction.

In the optical-model approximation the scattering state $\chi_a^{(+)}$ and $\chi_b^{(-)}$ are solutions of the Schrödinger equation:

$$[\nabla^2 + k^2 - \frac{2\mu}{\hbar^2} (U_c(r) + U(r))] \chi(\vec{k}, \vec{r}) = 0 \quad (4.3-2)$$

where $U(r)$ is the optical-model potential, $U_c(r)$ the coulomb potential, and μ the reduced mass of the pair.

In its most generalized form the optical-model potential is given by:

$$U(r) = -[Vf(r) + i Wg(r) + 4iW_D g'(r) + \lambda(\vec{S} \cdot \vec{L}) \frac{df}{dr}] \quad (4.3-3)$$

where $f(r)$, $g(r)$, and $g'(r)$ are the Wood-Saxon form factors given by:

$$f(r) = \frac{1}{1+e^{x_v}} \quad ; \quad x_v = \frac{r-r_v A^{1/3}}{a_v} \quad (4.3-4)$$

$$g(r) = \frac{1}{1+e^{x_w}} \quad ; \quad x_w = \frac{r-r_w A^{1/3}}{a_w} \quad (4.3-5)$$

$$g'(r) = \frac{e^{x_w}}{(1+e^{x_w})^2} \quad (4.3-6)$$

The first term of eqn. (4.3-3) corresponds to volume potential scattering, the second to volume potential absorption, the third to surface absorption and the fourth to spin-orbit scattering.

In the treatment of the $Ne^{20}(d,n)Na^{21}$ data the terms W and λ were set to zero, consistent with the ideas of a purely surface absorption interaction and negligible spin-orbit effect.

By setting λ (which in general is complex) equal to zero one can neglect the spin structure of the particles. The resulting wave function, $\chi_a^{(+)}$ and $\chi_b^{(-)}$, are then reduced from matrices to scalar functions and are related in the following way by the condition of time reversibility,

$$\chi^{(-)*}(\vec{k}, \vec{r}) = \chi^{(+)}(-\vec{k}, \vec{r}). \quad (4.3-7)$$

In performing the integration of eqn. (4.3-1) the scattering state wave functions are first expanded into a series of partial waves, i.e.:

$$\chi^{(+)}(\vec{k}, \vec{r}) = \frac{4\pi}{k} \sum_{L,M} i^L \chi_L(k,r) Y_L^{*M}(\hat{k}) Y_L^M(\hat{r}) \quad (4.3-8)$$

The resultant radial wave function, $\chi_L(k,r)$, is given by:

$$\left[\frac{d^2}{dr^2} + k^2 - \frac{L(L+1)}{r^2} - \frac{2\mu}{\hbar^2} (V(r) + iW_D(r) + U_C(r)) \right] \chi_L(k,r) = 0 \quad (4.3-9)$$

and takes on the asymptotic form:

$$\chi_L(k, r) = \frac{1}{2} [H_L^*(kr) - \eta_L H_L(kr)] e^{i\sigma_L} \quad (4.3-10)$$

where $H_L = (G_L + i F_L)$, the Coulomb functions irregular and regular at the origin; σ_L is the Coulomb phase shift; and η_L is the reflection coefficient for the L^{th} partial wave.

The remaining factor in eqn. (4.3-1) is the interaction matrix element, $\langle Bb | V | Aa \rangle$. This factor is a function of \vec{r}_a and \vec{r}_b and plays the role of an effective interaction for the transition between the elastic scattering states, χ_a and χ_b . It contains all the information on nuclear structure, angular momentum selection rules and even the type of reaction being considered (i.e. stripping, pickup, or inelastic scattering).

A number of general statements can be made about the matrix element by expanding it into terms where a definite angular momentum, \vec{j} , is transferred to nucleus A to form the residual nucleus B. That is

$$\vec{j} = \vec{j}_A - \vec{j}_B \quad (4.3-11)$$

where \vec{j} is made up of an orbital angular momentum transfer $\vec{\ell}$, and a spin part \vec{s} , given by:

$$\vec{s} = \vec{s}_a - \vec{s}_b \quad (4.3-12)$$

$$\vec{\ell} = \vec{j} - \vec{s} \quad (4.3-13)$$

The product $J\langle Bb|V|Aa\rangle$ is then expressed as:

$$\begin{aligned}
 J\langle Bb|V|Aa\rangle &= J\langle s_b m_b, J_B M_B | V | J_A M_A, s_a m_a \rangle \\
 &= \sum_{\ell s j} i^{-\ell} (-1)^{s_b - m_b} G_{\ell s j, m}(\vec{r}_b, \vec{r}_a; bB, aA) \\
 &\quad \times \langle J_A j M_A, M_B - M_A | J_B M_B \rangle \langle s_a s_b m_a - m_b | s m_a - m_b \rangle \\
 &\quad \times \langle \ell s m, m_a - m_b | j M_B - M_A \rangle \quad (4.3-14)
 \end{aligned}$$

where the Clebsch-Gordon coefficients take care of the angular momentum coupling, and where $m = M_B - M_A + m_a - m_b$. The notation, bB and aA , denotes the possible dependence of G on other nuclear and projectile quantum numbers and the factor $i^{-\ell}$ is included to ensure convenient time-reversal properties. Formally $G_{\ell s j, m}$ is defined by the inversion of eqn. (4.3-14) (Sa 64).

In general the function $G_{\ell s j, m}$ can be factored into an amplitude and a form factor:

$$G_{\ell s j, m}(\vec{r}_b, \vec{r}_a) = A_{\ell s j} f_{\ell s j, m}(\vec{r}_b, \vec{r}_a) \quad (4.3-15)$$

where the spectroscopic coefficient $A_{\ell s j}$ includes such quantities as fractional parentage coefficients and the interaction strength.

Summarizing the results to this point, eqn. (4.3-1) can now be written as

$$\begin{aligned}
 T_{Dw} &= \langle \vec{k}_b, J_B M_B, s_b m_b | V | \vec{k}_a, J_A M_A, s_a m_a \rangle \\
 &= \sum_{\ell s j} (2j+1)^{1/2} A_{\ell s j} \langle J_A j M_A, M_B - M_A | J_B M_B \rangle \beta_{s j}^{\ell m m_a m_b}(\vec{k}_b, \vec{k}_a) \\
 &\quad (4.3-16)
 \end{aligned}$$

where the "reduced" amplitude, β , is given by:

$$(2j+1)^{1/2} i^\ell \beta_{sj}^{\ell m} m_a m_b = (-1)^{s_b - m_b} \langle \ell s m, m_a - m_b | j M_B - M_A \rangle$$

$$\times \langle s_a s_b m_a - m_b | s m_a - m_b \rangle (2j+1)^{1/2} i^\ell \beta_{sj}^{\ell m} \quad (4.3-17)$$

and where,

$$(2j+1)^{1/2} i^\ell \beta_{sj}^{\ell m} = \int d\vec{r}_a \int d\vec{r}_b \chi_b^{*(-)}(\vec{k}_b, \vec{r}_b) f_{\ell s j, m}(\vec{r}_b, \vec{r}_a) \chi_a^{(+)}(\vec{k}_a, \vec{r}_a) \quad (4.3-18)$$

Referring to eqn. (4.3-18) we see that the integration over $d\vec{r}_a$ and $d\vec{r}_b$ is a six dimensional integral, which in general is a difficult task. To overcome this difficulty the zero-range approximation is introduced. In this approximation particle, b, is assumed to be produced at the same point that, a, is absorbed. Thus

$$\vec{r}_b = \frac{M_A}{M_B} \vec{r}_a \quad (4.3-19)$$

and

$$f_{\ell s j, m}(\vec{r}_b, \vec{r}_a) \rightarrow \delta\left(r_b - \frac{M_A}{M_B} r_a\right) f_{\ell s j, m}(\vec{r}_a) \quad (4.3-20)$$

The resultant integration is then reduced to a three dimensional integral.

It has been shown by Austern et al., (Au 64) that the zero-range approximation is valid if only small momentum components

of the distorted wave are important, characteristic of a surface interaction.

If we now incorporate the zero-range approximation and the partial wave expansion of eqn. (4.3-8) into the calculation of eqn. (4.3-18) we get, upon realizing the orthogonality of the spherical harmonics:

$$\beta_{sj}^{\ell m}(\theta) = \sum_{L_a L_b} \Gamma_{L_a L_b}^{\ell m} P_{L_b}^m(\theta) f_{L_a L_b}^{\ell sj}; m > 0 \quad (4.3-21)$$

where

$$\Gamma_{L_b L_a}^{\ell m} = i^{L_a - L_b - \ell} (2L_b + 1) \left[\frac{(L_b - m)!}{(L_b + m)!} \right]^{1/2} < L_b \ell 00 | L_a 0 > < L_b \ell m - m | L_a 0 > \quad (4.3-22)$$

and

$$f_{L_a L_b}^{\ell sj} = \frac{\sqrt{2\pi}}{k_a k_b} \frac{M_B}{M_A} \int \chi_{L_b}(k_b, \frac{M_A}{M_B} r) f_{\ell sj}(r) \chi_{L_a}(k_a, r) dr \quad (4.3-23)$$

and $P_L^m(\theta)$ is the associated Legendre polynomial of order L, m .

Two principal features characteristic of direct reactions are realized in eqn. (4.3-21), viz:

- (i) The shape of the angular distribution is given by an infinite sum of Legendre polynomials. However $f_{L_a L_b}^{\ell sj}$, quickly tends to zero for $L_a > k_a R$ and $L_b > k_b R$ (where R is the nuclear radius). The resultant truncated series then establishes the characteristic stripping shape.

(ii) The parity of the transition is given by

$(-1)^\ell$ as dictated by the requirement that $L_a + L_b + \ell$ be even in the Clebsch-Gordon coefficient, $\langle L_b \ell 00 | L_a 0 \rangle$.

The differential cross-section for unpolarized projectiles and unpolarized target nuclei is given by

$$\frac{d\sigma}{d\Omega} = \frac{\mu_a \mu_b}{(2\pi\hbar^2)^2} \frac{k_b}{k_a} \frac{\sum |T|^2}{(2J_A + 1)(2S_a + 1)}$$

where μ_a and μ_b are the reduced masses of the respective pairs, and the sum is over M_A , m_a , M_B , and m_b . Upon substituting for T (eqn. 4.3-16); summing over M_A , m_a , M_B , and m_b ; and realizing the orthogonality properties of the Clebsch-Fordon coefficients, eqn. (4.3-24) becomes:

$$\frac{d\sigma}{d\Omega} = \frac{\mu_a \mu_b}{(2\pi\hbar^2)^2} \frac{k_b}{k_a} \frac{2J_B + 1}{(2J_A + 1)(2S_a + 1)} \sum_{\ell sj, m} |A_{\ell sj}|^2 |\beta_{sj}^{\ell m}|^2 \quad (4.3-25)$$

It will be noted that in the resultant expression, eqn. (4.3-25), the contributions from ℓ , s , and j are all incoherent. This is not the case when the effects of spin-orbit coupling are considered. Then only the j summation is incoherent (Sa 64).

The results developed to this point are applicable to direct reactions in general (i.e. stripping, pickup, inelastic scattering, etc.). Let us now specialize the treatment to the single nucleon stripping reactions characterized by, $A(d,n)B$, i.e.:

$$\vec{r}_a \rightarrow \vec{r}_d \quad (4.3-26)$$

$$\vec{r}_b \rightarrow \vec{r}_n \quad (4.3-27)$$

$$V \rightarrow V_{np}. \quad (4.3-28)$$

The choice of interaction potential, V_{np} , (i.e. the neutron-proton interaction) is based on the following approximation.

As viewed in the recoil channel, the total interaction potential is given by:

$$V_T = V_{nB} = V_{np} + V_{pA}. \quad (4.3-29)$$

The residual interaction, V , is given by subtracting off the optical potential, U_{nB} :

$$V = V_{np} + V_{pA} - U_{nB}; \quad (4.3-30)$$

and is approximated by the central-force potential

$$V = V_{np}. \quad (4.3-31)$$

The nuclear matrix element of eqn. (4.3-1) can now be written as:

$$\begin{aligned} J \langle Bn | V | Ad \rangle &= J \int d\xi_A \phi_B^{*J_B M_B}(\vec{r}_{pA}, \sigma_p, \xi_A) \phi_n^{* \frac{1}{2} M_{\frac{1}{2}}}(\sigma_n) \\ &\times V(r_{np}) \phi_A^{J_A M_A}(\xi_A) \phi_d^{l m l}(\vec{r}_{np}, \sigma_p, \sigma_n), \end{aligned} \quad (4.3-32)$$

where ξ_A represents the internal coordinates of A; σ_p the spin structure of the captured proton; and σ_n the spin structure of

the emitted neutron. The Jacobian, J , corresponds to the transformation from the coordinates r_{pA} and r_{np} to r_n and r_d , and is given by

$$J = \left[\begin{array}{cc} M_d & M_a \\ M_p & (M_d + M_A) \end{array} \right]^3 \quad (4.3-33)$$

To evaluate the matrix element of eqn. (4.3-32) the following forms for the wave functions are usually taken.

(i) The nuclear wave function ϕ_B is expanded into a fractional parentage expansion over the eigenstates of the target nucleus and the single particule state of the captured proton, i.e.:

$$\begin{aligned} \phi_B^{J_B M_B}(\vec{r}_{pA}, \sigma_p, \xi_A) &= \sum_{j \mu J_A' M_A'} \phi_A^{J_A' M_A'}(\xi_A) \Omega_j^{B A'}(r_{pA}, \sigma_p) \\ &\times \langle J_A' j M_A' | J_B M_B \rangle. \end{aligned} \quad (4.3-34)$$

The function Ω_j may be regarded as proportional to the single particle wave function of the captured proton. It can be

separated into its radial, orbital, and spin components in the following way,

$$\Omega_{j\mu}^{BA'}(\vec{r}_{pA}, \sigma_p) = \sum_{\ell sm} n^{\frac{1}{2}} \alpha_{\ell j}^{BA'} \mu_{\ell j}(r_{pA}) i^{\ell} Y_{\ell}^m(\tilde{r}_{pA}) \phi_{s, \mu-m}(\sigma_p) \times \langle \ell sm, \mu - m | j \mu \rangle \quad (4.3-35)$$

The number n equals the number of equivalent nucleons in the orbital and is introduced to antisymmetrize the wave function. The coefficient, $\alpha_{\ell j}$, is the fractional parentage coefficient and the product,

$$S_{\ell j} = n(\alpha_{\ell j})^2 \quad (4.3-36)$$

is the spectroscopic factor. It is a measure of the probability that the final nucleus is made up of the configuration of the target nucleus and the captured particle in the single particle state.

(ii) The neutron is considered as an elementary particle with no internal structure, and is given by the normalized spin function:

$$\phi_n^{\frac{1}{2} m_{\frac{1}{2}}}(\sigma_n). \quad (4.3-37)$$

(iii) Only the S state structure of the deuteron is considered, which makes it factorable into the product of a

Hulthen wave function and a spin function, i.e.:

$$\begin{aligned}\phi^{1m_1}(r_{np}, \sigma_p, \sigma_n) &= N \left[\frac{e^{-\alpha r_{np}} - e^{-\beta r_{np}}}{r_{np}} \right] \phi_{1m_1}(\sigma_p, \sigma_n) \\ &= \phi_d(r_{np}) \phi_{1m_1}(\sigma_p, \sigma_n)\end{aligned}\quad (4.3-38)$$

where the normalization coefficient is given by,

$$N = \left[\frac{\alpha\beta(\alpha + \beta)}{\pi(\beta - \alpha)} \right]^{\frac{1}{2}}. \quad (4.3-39)$$

The parameter, α , is given by:

$$\alpha = \frac{\sqrt{M\varepsilon_d}}{\hbar^2}, \quad (4.3-40)$$

where M equals the average of the neutron and proton mass and ε is the binding energy of the deuteron ($\varepsilon = 2.2245$ Me V.). The parameter β is usually taken as

$$\beta = 7\alpha. \quad (4.3-41)$$

Using the above forms for the respective wave functions the matrix element, eqn. (4.3-32) can now be evaluated. Since the interaction potential, $V(r_{np})$, does not depend on the coordinates, \vec{r}_{pA} , the orthogonality condition demands that the only contributing state of the target nucleus is, $J'_A = J_A$ and

$M'_A = M_A$. Thus, upon expanding the spin structure of the deuteron into the spin structure of the neutron and proton and coupling the composite spin to the value, s , eqn. (4.3-32) can be written as:

$$\begin{aligned}
 J\langle B, n | V_{np} | A, d \rangle &= J \sum_{\ell s j} i^{-\ell} (-1)^{s_n - m_n} \langle J_A j M_A, M_B - M_A | J_B M_B \rangle \\
 &\times \langle \ell s m, m_d - m_n | j M_B - M_A \rangle \langle s_d s_n m_d - m_n | s m_d - m_n \rangle \\
 &\times \frac{\sqrt{2 S_d + 1}}{2S + 1} n^{\frac{1}{2}} \alpha_{\ell j} \mu_{\ell j}(r_{pA}) Y_{\ell}^{*m}(\tilde{r}_{np}) V(r_{np}) \phi_d(r_{np}) \quad (4.3-42)
 \end{aligned}$$

where $m = M_B - M_A + m_d - m_n$.

Upon comparing eqn. (4.3-42) with eqn. (4.3-14) we see that,

$$G_{\ell s j, m} = \frac{\sqrt{2 S_d + 1}}{2S + 1} n^{\frac{1}{2}} \alpha_{\ell j} \mu_{\ell j}(r_{pA}) Y_{\ell}^{*m}(\tilde{r}_{np}) V(r_{np}) \phi_d(r_{np}) \quad (4.3-43)$$

where consistent with the ideas of eqn. (4.3-15) we make the separation:

$$A_{\ell s j} = \frac{\sqrt{2 S_d + 1}}{2S + 1} n^{\frac{1}{2}} \alpha_{\ell j} V(r_{np}) \phi_d(r_{np}) \quad (4.3-44)$$

$$f_{\ell j} = \mu_{\ell j}(r_{pA}). \quad (4.3-45)$$

The zero-range approximation is introduced by writing,

$$V(r_{np})\phi_d(r_{np}) = D_o \delta(r_{np}) \quad (4.3-46)$$

with

$$D_o = \int V_{np}(r)\phi_d(r)dr. \quad (4.3-47)$$

The radial wave functions of the captured proton, $\mu_{\ell j}(r_{pA})$, are usually taken as eigensolutions of the Schrödinger equation for a potential well of the Wood-Saxon type (eqn. (4.3-4)). The parameters used (V_o , r_o , and a) are usually those taken from proton elastic scattering work.

In the event that the stripped proton is captured into a nuclear orbital of defined spin and parity charge, the summation over ℓ and s , in eqn. (4.3-39), is superfluous (i.e., $s = \frac{1}{2}$ and $\ell = j \pm \frac{1}{2}$ as dictated by the parity change). Also from the structure of eqn. (4.3-42) we see that the following selection rules apply:

- (i) the parity change is given by $(-1)^\ell$ as dictated by the presence of the Y_ℓ^m , and
- (ii) the final spin value, J_B , as limited by the Clebsch-Gordon coefficients, is:

$$|J_A - \ell - \frac{1}{2}| \leq J_B \leq J_A + \ell + \frac{1}{2}. \quad (4.3-48)$$

(ii) The D.W.B.A. Angular Distributions

A program, written by B. E. F. Macefield (Ma 64) and

embodying the theory of the preceeding section, was used to calculate the angular distributions corresponding to the formation of the ground, 0.335, 1.751, and 2.433 levels of Na^{21} via the $\text{Ne}^{20}(\text{d}, \text{n})\text{Na}^{21}$ reaction. A local, Wood-Saxon optical potential (eqn. 4.3-3) (with zero volume absorption and spin-orbit terms) was used to evaluate the scattering state wave functions. In addition the zero-range approximation was used throughout.

The average optical potential parameters given by Perey and Buck (Ro 66) were used for the neutron wave functions. However, the corresponding parameters for the deuteron were not as easily obtained. A literature search revealed that no optical model analysis had ever been done for the elastic scattering of deuterons off Ne^{20} and that the closest relevant work was some elastic scattering data at 10.95 MeV. (Ta 60) and 11.6 MeV. (Ja 65). Working under the assumption that the energy difference between the elastic scattering data and the reaction data could be accounted for by a small variation in V , the above data was subsequently analysed by an optical-model search code, written by C. M. Perey (Ob66). A total of five optimum fits, ranging in V value from 58.0 MeV. to 170.0 MeV., were obtained for the two sets of data. (The corresponding variation in the other parameters was not significant.)

When the aforementioned sets of deuteron parameters were

substituted into the D.W.B.A. program little change in shape was predicted, however, a 20% change in magnitude was noted. Since this produced a corresponding 20% variation in the spectroscopic factors it became necessary to single out a unique set of deuteron parameters. This was achieved by appealing to the hypothesis that the real part of the optical potential, for a deuteron, should be near the sum of the neutron and proton potentials. This would place it near 100 MeV.

Deuteron parameters of near equal value, for the two different sets of data (10.95 and 11.6 MeV data), were then averaged and the results closest to a real potential value of 100 MeV was chosen. The results so selected corresponded to a real potential value of 121.995 MeV.

In an effort to improve the D.W.B.A. fits a search through V was made. This was consistent with the idea that the difference in energy between the scattered and reaction data could be accounted for by a variation in V . A marginal degree of improvement was achieved by using a real potential value of 95.0 MeV.

Figs. 4-4 and 4-5 illustrate respectively the results of the elastic scattering analysis and the D.W.B.A. calculations, while Tables 4-6 and 4-7 summarize the potentials used.

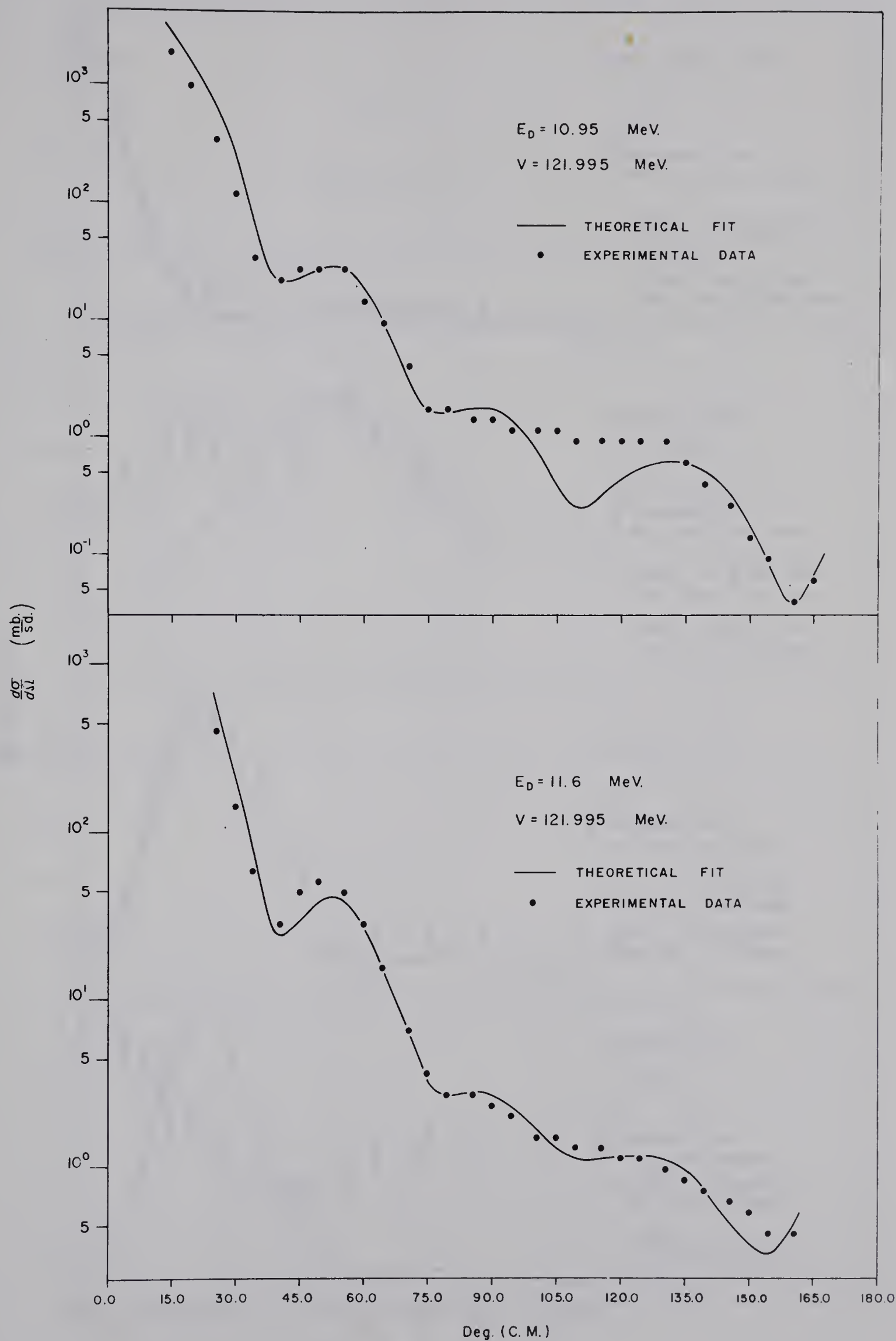


Fig. 4-4: $\text{Ne}^{20}(\text{d},\text{d})\text{Ne}^{20}$ Elastic Scattering

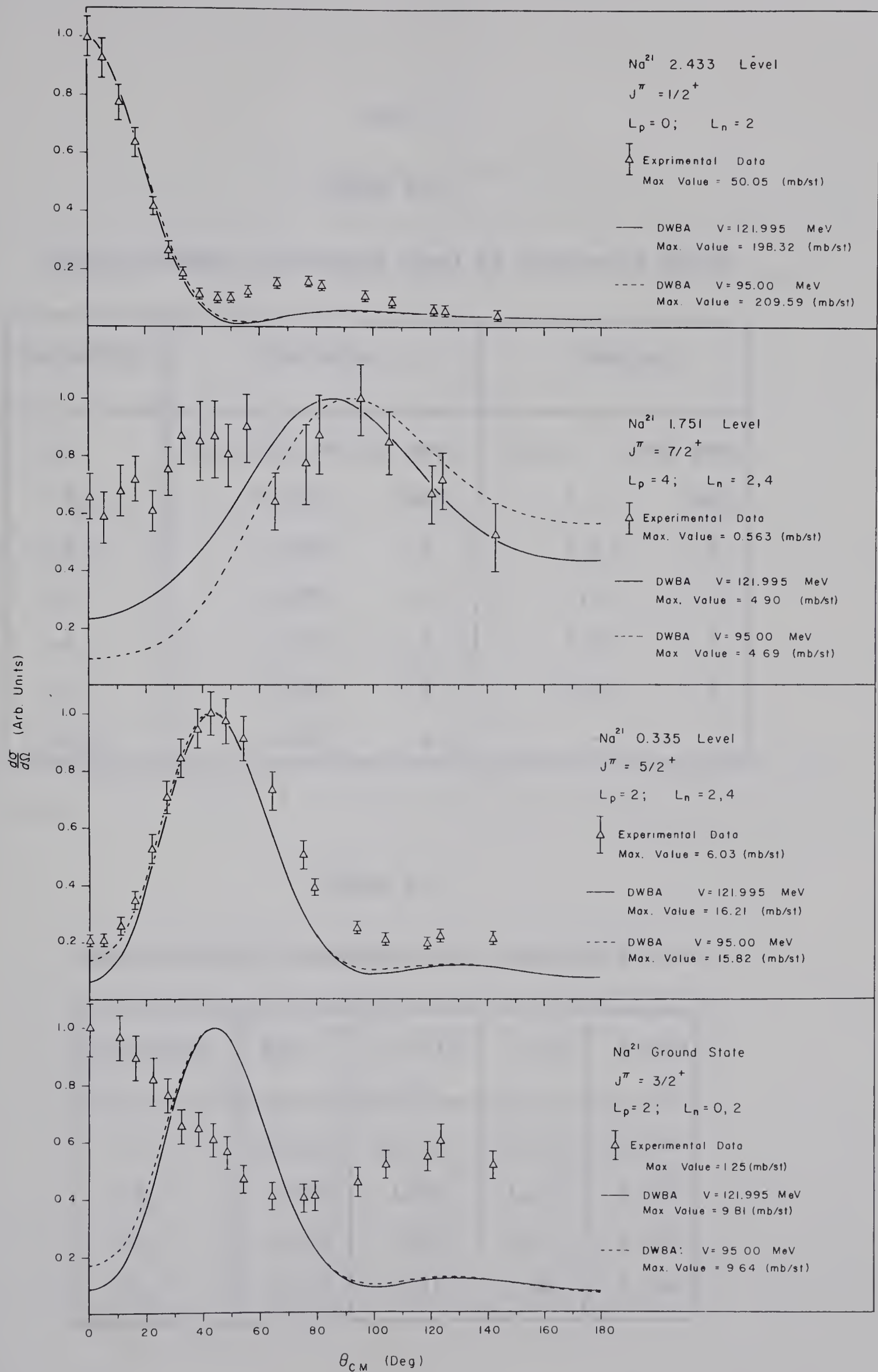


Fig. 4-5: Neutron Angular Distributions

Table 4-6

Optical-Model Parameters used by Scattered Waves

Parameter	Deuteron	Neutron
V	121.995; 95.00 MeV.	48.0 - 0.29E MeV.
W_D	25.721 MeV.	9.6 MeV.
R_r	1.228 f.	1.27 f.
R_i	1.291 f.	1.27 f.
a_r	0.671 f.	0.66 f.
a_i	0.625 f.	0.47 f.
R_c	1.300 f.	-

Table 4-7

Optical-Model Parameters for Captured Proton

Parameter	gnd.	0.335	1.751	2.433
V	56.22	55.59	65.14	50.28
R_r	1.25	1.25	1.70	1.25
a_r	0.65	0.65	0.65	0.65
R_c	1.30	1.30	1.30	1.30

Referring to Fig. 4-5 we see that only the 0.335; 2.433; and, to a lesser extent, the 1.751 levels are characterized by the stripping mechanism (and thus validate the corresponding spin and parity assignments) whereas, the ground state is not so described. A valid determination of the shape of the 1.751 level is hampered by a very low cross section (0.563 mb/st. at 95.86°).

Spectroscopic factors for the 0.335, 1.751, and 2.433 levels are given in Table 4-8 and were obtained from the equation,

$$\frac{d\sigma}{d\Omega}(\theta) = 1.48 \frac{2J_f + 1}{2J_i + 1} S \sigma(\theta)_{s.p.} \quad (4.3-49)$$

where $\frac{2J_f + 1}{2J_i + 1} \sigma(\theta)_{s.p.}$ is the output value given by Macefield's program. The factor 1.48 comes from the Hulthen wave function.

Table 4-8

Spectroscopic Factors

Deuteron Potential	Nuclear Level	Max. $\frac{d\sigma}{d\Omega}$ (exp't.) ($\frac{mb}{st}$)	Max. $\frac{d\sigma}{d\Omega}$ (Ma.) ($\frac{mb}{st}$)	S
$V_d = 121.995$	0.335	6.03 (43.88°)	16.21 (44.0°)	0.37
	1.751	0.563 (95.86°)	4.90 (85.0°)	0.11
	2.433	50.05 (0°)	198.32 (0°)	0.25

Table 4-8 (continued)

Deuteron Potential	Nuclear Level	Max. $\frac{d\sigma}{d\Omega}$ (exp't.) ($\frac{\text{mb}}{\text{st}}$)	Max. $\frac{d\sigma}{d\Omega}$ (Ma.) ($\frac{\text{mb}}{\text{st}}$)	S
$V_d = 95.00$	0.335	6.03 (43.88°)	15.82 (42.0°)	0.38
	1.751	0.563 (95.86°)	4.69 (90.0°)	0.12
	2.433	50.05 (0°)	209.59 (0°)	0.24

4.4 Discussion

(i) Approximations made in the D.W.B.A. analysis

Referring to Fig. 4-5, we see that even for those levels exhibiting stripping structure the fits are far from ideal. There is justification for this inconsistency, however, when one realizes the many approximations made in the D.W.B.A. theory, viz:

- (i) no contribution due to compound reaction formation was considered;
- (ii) only first order perturbation theory was used (eqn. 4.3-1);
- (iii) no volume absorption or spin-orbit effects were included in evaluating the scattering state wave functions;
- (iv) the optical potentials giving rise to the scattering state wave functions

- were assumed to be local potentials;
- (v) the zero-range approximation was used throughout;
 - (vi) the interaction potential, V , was reduced to a central-force, neutron-proton interaction;
 - (vii) only the S state structure of the deuteron was considered; and
 - (viii) the captured proton radical wave functions, $u_{\ell j}(r_{pA})$, were taken as solutions of a spherically symmetric potential characteristic of shell structure, whereas, in the case of deformed nuclei, such as Na^{21} , a non-spherical potential is required.

Of the approximations listed, number (i) can contribute the greatest error to both the shape and magnitude of the angular distribution. For in reality, the true transition amplitude consists of two terms, viz:

$$T = T_D + T_C \quad (4.4-1)$$

where T_D refers to direct reaction formation and T_C to compound reaction formation. Then referring to eqn. (4.3-24), the differential cross section becomes

$$\frac{d\sigma}{d\Omega} \propto \sum_i \left[|T_D^i|^2 + |T_C^i|^2 + \cos \phi_i T_D^i T_C^i \right] \quad (4.4-2)$$

(where i refers to the spin substates). Thus if compound reaction formation is not negligible, the effects of $|T_C|^2$ and the interference terms can alter significantly the shape and magnitude of the angular distribution.

Point number (viii) is the second source of major error, and results in a spectroscopic factor smaller than would be expected from the Nilsson wave function formalism. The remaining approximations tend to be of secondary effect.

(ii) The absence of stripping structure in the formation of the ground state of Na^{21}

The most identifying feature of the results of Fig. 4-5 is the absence of stripping structure in the formation of the ground state of Na^{21} . On the basis of the D.W.B.A. theory of section 4.3 the shape of an angular distribution, for single nucleon capture into a state of well defined spin and parity, is determined primarily by the ℓ value of the captured nucleon. Since the ground state of Na^{21} has a well defined spin and parity value, characteristic stripping structure should be evident. One reconciles this anomaly by appealing to the following argument.

If the state excited is poorly defined as a single particle

level a small spectroscopic factor, and thus direct reaction component of the transition amplitude, is predicted. The presence of any compound reaction formation then becomes significant and assumption (i), of the previous section breaks down. The generalized expression for the differential cross section, eqn. (4.4-2), must then be employed, with a resultant variation in the shape of the angular distribution.

One can say qualitatively from the poor agreement between the theoretical and experimental angular distributions, for the ground state, that the compound reaction component of the transition amplitude appears to be the dominate term. This argument may well apply to the 1.751 level also.

(iii) Collective model interpretation of Na^{21}

The collective model interpretation has been applied with a high degree of success to Na^{21} and other nuclei in the 1d-2s shells: (Bh62), (Ch63), and (Ho65). In the case of Na^{21} the deformed core consists of 10 protons and 10 neutrons coupled to an equilibrium shape of a prolate spheroid. The remaining single proton is thought of as orbiting this core under the influence of a non-spherical potential.

The Hamiltonian describing such a system is given by,

$$H = H_{\text{rot}} + H_o \quad (4.4-3)$$

where H_{rot} refers to the collective rotational motion of the deformed core and H_o refers to the single-particle motion of the extra-core nucleons. In explicit form these terms are given by:

$$H_{\text{rot}} = \frac{\hbar^2}{2I} \left[J(J+1) - K^2 - \Omega^2 \right] + \frac{\hbar^2}{2I_3} (K-\Omega)^2 - \frac{\hbar^2}{2I} (J_{+j-} + J_{-j+}) \quad (4.4-4)$$

and

$$H_o = \sum_p H_p + \frac{\hbar^2}{2I} \left(\sum_p \vec{j}_p \right)^2 \quad (4.4-5)$$

where J is the total spin of the nucleus, j is the composite spin of the extra-core nucleons, K is the projection of J onto the body fixed 3-axis, Ω is the projection of j onto the body fixed 3-axis, and I is the moment of inertia of the deformed core. The rotational-particle coupling (R.P.C.) operator, $J_{+j-} + J_{-j+}$, serves to couple together states of different K value, namely $\Delta K = \pm 1$ ($\Delta K = 0$ if $K = \frac{1}{2}$). The sum in eqn. (4.4-5) is usually reduced to just one particle by dropping the inter-particle coupling term $\vec{j}_p \cdot \vec{j}_q$.

If one ignores the R.P.C. term of eqn. (4.4-4) and makes the assumption of a rotationally symmetric deformation, i.e., $K = \Omega$ (a feature characteristic of low lying levels) one gets

for the resultant properly normalized and symmeterized* solution of the composite system,

$$|JM\Omega\pi\alpha\rangle = \left[\frac{2J+1}{16\pi^2} \right]^{\frac{1}{2}} \left[D_{M\Omega}^J | \Omega\pi\alpha\rangle + (-1)^{J-j} D_{M-\Omega}^J | -\Omega\pi\alpha\rangle \right] \quad (4.4-6)$$

where

$$H_0 | \Omega\pi\alpha\rangle = \epsilon_\Omega | \Omega\pi\alpha\rangle. \quad (4.4-7)$$

The eigensolutions, $| \Omega\pi\alpha\rangle$, form what are known as the Nilsson model wave functions, where π is the parity of the single particle level and α is the Nilsson orbital number. In the shell model limit the potential used by H_0 becomes spherically symmetric and the corresponding eigensolutions become the degenerate shell model wave functions parameterized by μ (the strength of the ℓ^2 splitting term) and κ (the strength of the spin-orbit coupling). For the Nilsson wave functions the additional parameter, η , is introduced as a measure of the deformation; and since a well defined axis exists for deformed nuclei, namely the symmetry axis, the spin degeneracy is removed and $\Omega (= K)$ becomes a constant of motion.

In evaluating the wave functions $| \Omega\pi\alpha\rangle$ a spherical-limit,

* One symmeterizes the wave function with respect to reflection in the equatorial plane.

shell model expansion is usually made, i.e.:

$$|\Omega\pi\alpha\rangle = \sum_{N\ell j} \langle N\ell j | \Omega\pi\alpha \rangle |N\ell j\rangle \quad (4.4-8)$$

where $|N\ell j\rangle$ form a basis set of shell model wave functions characterized by the phonon number N , orbital angular momentum ℓ , and composite spin j ; and where $\langle N\ell j | \Omega\pi\alpha \rangle$ are the expansion coefficients. The summation in eqn. (4.4-8) is usually restricted to a single oscillator shell, i.e., one N value.

With the above forms taken as eigensolutions, the eigenvalues of eqn. (4.4-3) become,

$$E(J, \Omega) = \epsilon_{\Omega} + \frac{\hbar^2}{2I} \left[J(J+1) - 2\Omega^2 + \delta_{\Omega\frac{1}{2}} a (-1)^{J+\frac{1}{2}} (J+\frac{1}{2}) \right] \quad (4.4-9)$$

where, a , known as the decoupling parameter, is given by

$$a = - \sum_j \langle N\ell j | \Omega\pi\alpha \rangle^2 (j+\frac{1}{2}) (-1)^{j+\frac{1}{2}}. \quad (4.4-10)$$

The values ϵ_{Ω} have been calculated numerically and are summarized, for orbits of interest, by the Nilsson diagram of Fig. 4-6 (Ho65).

From eqn. (4.4-9) we see that, for a given $\Omega (\Omega \neq \frac{1}{2})$, the rotational bands are built upon the respective single particles levels with spin predictions given by $J = \Omega, \Omega + 1, \Omega + 2, \dots$. With this knowledge the following interpretation of the level structure of Na^{21} can be made.

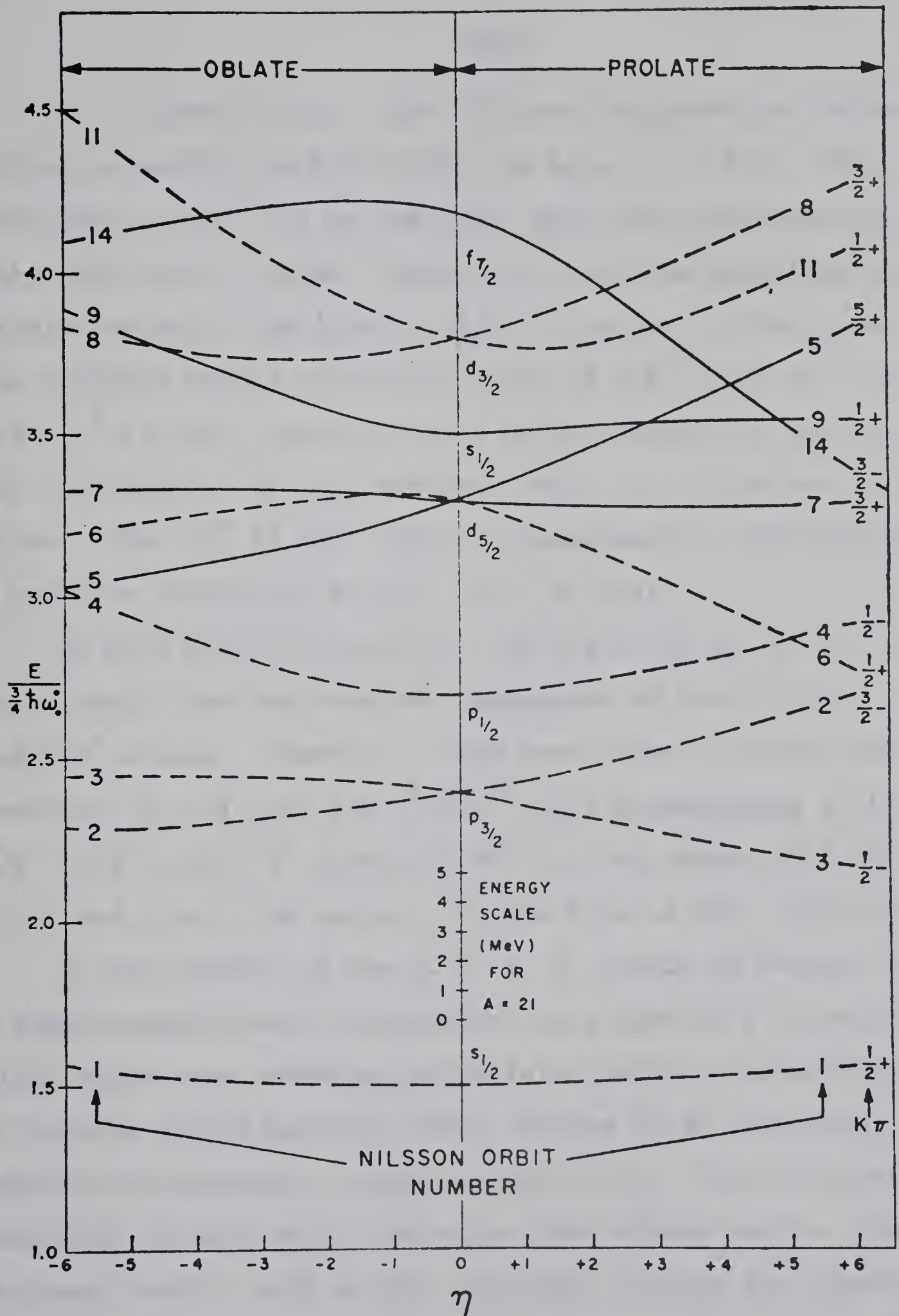


Fig. 4-6: Nilsson Diagram

A. J. Howard et al., (Ho 65) have estimated the deformation parameter for A=21 nuclei as being, $\eta = 4.0$. With reference to Fig. 4-6 we see that, with four nucleons going into each level, the Na^{21} nucleus can then be described by a single proton in the $|\Omega\pi\alpha\rangle = |3/2 + 7\rangle$ state. This gives the required ground state spin value of $3/2^+$. The $5/2^+$ (0.335) and $7/2^+$ (1.751) levels can then be interpreted as the $\Omega+1$ and $\Omega+2$ elements of the rotational band built upon the $|3/2+7\rangle$ state. The $1/2^+$ (2.433) level is subsequently interpreted as a particle excitation to the $|1/2 + 9\rangle$ state.

To this point the analysis has neglected the R.P.C. term which would then mix together components of the $\Omega^\pi=3/2^+$, $1/2^+$, and $5/2^+$ states. However, it has been shown by Kelson and Levinson (Ke 64) that the $\Omega^\pi=3/2^+$ state predominates in the $3/2^+$, $5/2^+$, and $7/2^+$ levels of Na^{21} to the amount of 0.98, 0.85, and 0.80. The neglect of this term is then justified.

In the context of the D. W. B. A. theory of Section 4.3, a spectroscopic factor represents the probability to which the final state wave function can be interpreted as consisting of an extreme single particle level coupled to an unexcited, spherically-symmetric, target-nucleus core. Such an interpretation is only valid for nuclei near closed shells. For deformed nuclei, such as Na^{21} , one must account for possible rotational and vibrational motion of the core in addition to introducing non-spherical potentials for the extra-core nucleons.

Following the outline of Satchler (Sa 58) the theory is modified in the following way.

Referring to eqn. (4.3-32) we see that under the assumption that $V=V(r_{np})$ only, the quantity of interest becomes the overlap integral between the target and residual nuclear wave functions, i.e.:

$$\int \psi_{J_B M_B}^*(r_{pA}, \xi) \psi_{J_A M_A}(\xi) d\xi = \sum_{j\ell} \sqrt{n} \beta_{j\ell} \phi_{j\ell m}(r_{pA}) \langle J_A j M_A m | J_B M_B \rangle \quad (4.4-11)$$

where once again we have made a fractional parentage expansion and $\phi_{j\ell m}$ representing the wave function of the captured proton. And as before the spectroscopic factor is given by,

$$S_{\ell j} = n \beta_{\ell j}^2. \quad (4.4-12)$$

In evaluating the overlap integral of eqn. (4.4-11) we make the following substitutions for the nuclear wave functions:

$$\psi_{J_A M_A}(\xi) = \left[\frac{2J_A + 1}{16\pi^2} \right]^{\frac{1}{2}} \left[D_{M_A K_A}^{J_A} | \Omega \pi \alpha \rangle_A + (-1)^{J_A - j_A} D_{M_A - K_A}^{J_A} | -\Omega \pi \alpha \rangle_A \right] \phi_{Vib}^A \quad (4.4-13a)$$

$$\begin{aligned} \psi_{J_B M_B}(\xi, r'_{pA}) = & \left[\frac{2J_B + 1}{16\pi^2} \right]^{\frac{1}{2}} \left[D_{M_B K_B}^{J_B} | \Omega \pi \alpha r'_{pA} \rangle_B \right. \\ & \left. + (-1)^{J_B - j_B} D_{M_B - K_B}^{J_B} | -\Omega \pi \alpha r'_{pA} \rangle_B \right] \phi_{Vib}^B. \end{aligned} \quad (4.4-13b)$$

(For the sake of generality we have assumed that $K \neq \Omega$, and have also accommodated any vibration structure via ϕ_{Vib} .)

Before performing the integration of eqn. (4.3-11) one must realize that states $|\Omega\pi\alpha r'_{pA} \rangle_B$ are related to the body fixed coordinate system, whereas, the function $\phi_{j\ell m}(r_{pA})$ is related to the space fixed system. This inconsistency is brought into line by realizing that:

$$\phi_{j\ell m}(r_{pA}) = \sum_{m'} D_{mm'}^j \phi_{j\ell m'}(r'_{pA}) \quad (4.4-14)$$

Thus the integral of interest is,

$$\sum_{m'} \int \psi_{J_B M_B}^*(r_{pA}, \xi) \psi_{J_A M_A}(\xi) D_{mm'}^j d\xi \quad (4.4-15)$$

Satchler has shown (Sa 58) that the results of such an integration yield,

$$\sqrt{S_{j\ell}(K_A \Omega_A, K_B \Omega_B)} = g \left[\frac{2J_A + 1}{2J_B + 1} \right]^{\frac{1}{2}} \langle J_A j \mp K_A, \Omega_B \mp \Omega_A | J_B K_B \rangle$$

$$x \langle N\ell j | \Omega_B \mp \Omega_A \pi\alpha \rangle \langle \phi_B | \phi_A \rangle \quad (4.4-16)$$

where $g = \sqrt{2}$ if either $K_A = \Omega_A = 0$ or $K_B = \Omega_B = 0$, and unity otherwise. The \mp is taken according to whether the captured proton enters an orbit with $\Omega = |\Omega_B \mp \Omega_A|$. The selection rule provided by the Clebsch-Gordon coefficient is:

$$K_A \mp K_B = \Omega_A \mp \Omega_B. \quad (4.4-17)$$

Since most ground states are characterized by $K_A = \Omega_A$

this requires that $K_B = \Omega_B$. Thus stripping to highly excited states, characterized by, $K_B \neq \Omega_B$, would consequently be retarded.

In the situation corresponding to the $\text{Ne}^{20}(\text{d},\text{n})\text{Na}^{21}$ reaction a proton of defined j, ℓ is captured by an even-even nucleus for which $J_A = K_A = \Omega_A = 0$. Eqn. (4.4-16) then reduces to,

$$S_{j\ell} = \frac{2}{2j+1} \langle N\ell j | \Omega\pi\alpha \rangle^2 \quad (4.4-18)$$

where the overlap integral between the vibration states, $\langle \phi_B | \phi_A \rangle$, has been set equal to unity consistent with the interpretation of the low-lying structure of Na^{21} .

Thus by exciting successive levels of a given rotational band one is able to explore the corresponding expansion coefficients of the Nilsson model wave function. And since $\langle N\ell j | \Omega\pi\alpha \rangle^2$ represents the probability, that in a measurement, the eigenstate $|\Omega\pi\alpha\rangle$ will be found in the state $|N\ell j\rangle$, the classical interpretation of a spectroscopic factor still applies.

Upon applying eqn. (4.4-18) to the spectroscopic data of Table 4-8, one gets (realizing that the 1d-2s shells are characterized by $N=2$):

$$\langle 2 \ 2 \ 5/2 | 3/2+7 \rangle^2 = 1.12 \quad (4.4-19)$$

$$\langle 2 \ 4 \ 7/2 | 3/2+7 \rangle^2 = 0.46 \quad (4.4-20)$$

$$\langle 2 \ 0 \ 1/2 | 1/2+9 \rangle^2 = 0.25 \quad (4.4-21)$$

An important conclusion, relating to the $\text{Ne}^{20}(\text{d},\text{n})\text{Na}^{21}$ experiment, can now be made.

Since the basis vectors $|N\ell j\rangle$ form a complete set of functions for a given N value,

$$\sum_{\ell j} \langle N\ell j | \Omega\pi\alpha \rangle^2 = 1. \quad (4.4-22)$$

The results of eqns. (4.4-19) and (4.4-20) then indicate that, within the framework of a purely direct-reaction formulation, the measured cross sections for the 0.335 and 1.751 levels are too high. This anomaly can be attributed to the lack of attention paid to the compound reaction component of the transition amplitude.

If one makes a number of simplifying assumptions, the results of eqns. (4.4-19), (4.4-20), and (4.4-22) can be used to estimate a minimum value for the average compound-reaction contribution to the angular distributions of the 0.335 and 1.751 levels.

First, let us assume that the direct reaction and compound reaction components of the transition amplitude add incoherently. Second, let us assume that the $|\Omega\pi\alpha\rangle = |3/2+7\rangle$ state is made up of only the $|N\ell j\rangle = |2\ 2\ 5/2\rangle$ and $|2\ 4\ 7/2\rangle$ basis vectors. (This corresponds to assuming that the Na^{21} ground state is formed wholly via the compound reaction mechanism and that higher ℓ value components of the basis set are negligible.) Our expansion of interest is then:

$$|3/2+7\rangle = \langle 2 \ 2 \ 5/2 \mid 3/2+7\rangle \mid 2 \ 2 \ 5/2\rangle \\ + \langle 2 \ 4 \ 7/2 \mid 3/2+7\rangle \mid 2 \ 4 \ 7/2\rangle, \quad (4.4-23)$$

for which

$$\langle 2 \ 2 \ 5/2 \mid 3/2+7\rangle^2 + \langle 2 \ 4 \ 7/2 \mid 3/2+7\rangle^2 = 1. \quad (4.4-24)$$

If we now assume that the average compound-reaction component is a constant value, for both the 0.335 and 1.751 levels, we get (using the results of Table 4-8, eqn. (4.4-18) and eqn. (4.4-24)):

$$\frac{2(5/2)+1}{2} \left[\frac{6.03-c}{16.01} \right] + \frac{2(7/2)+1}{2} \left[\frac{0.563-c}{4.79} \right] = 1, \quad (4.4-25)$$

for which the average background, compound-reaction component is:

$$c \approx 0.6 \text{ mb/st} \quad (4.4-26)$$

This result then forces one to interpret the 1.751 level as being formed entirely by the compound reaction mechanism, and also attributes a 10% compound reaction contribution to the 0.335 level.

Of the assumptions made, in this rather over-simplified analysis, that of an equivalent compound reaction contribution to both the 0.335 and 1.751 levels is perhaps, in first thought, the least intuitively justified. One might argue that, since

the ℓ_p value for the captured proton is 4 for the 1.751 level and only 2 for the 0.335 state, momentum transfer probabilities would be greater for the 0.335 level than for the 1.751. Such an argument is consistent with the idea that the proton-target interaction distance, r_{pA} , must be greater for $\ell_p=4$ capture than for $\ell_p=2$ (as dictated by the classical condition that $\ell_p = k_p r_{pA}$).

Such an argument is indeed valid, within the framework of the direct reaction formalism, and serves to account for the reduced cross-section of the 1.751 level. However, within the compound reaction formalism, we are involved with the complete absorption of the deuteron followed by the subsequent emission of a neutron. That is, a new point of view is taken and the angular momentum arguments must be altered accordingly. The conditions of interest here are the conservation of channel spin and parity.

If we assume that the compound nucleus, Na^{22} , is formed primarily by S-wave deuterons (which is consistent with the idea of the complete absorption of a rather large nucleus at a bombarding energy of 3.924 MeV) then the entrance channel spin and parity value are:

$$\vec{S}_i = \vec{L}_d + \vec{S}_d + \vec{J}_{Ne^{20}} = 1 \quad (4.4-27)$$

$$\Pi_i = (-1)^{L_d} \Pi_d \Pi_{Ne^{20}} = +1. \quad (4.4-28)$$

The conservation of channel spin allows, respectively for the ground, 0.335, 1.751, and 2.433 levels, angular momentum values of:

$$L_n(\text{gnd}) = 0, 1, 2, 3 \quad (4.4-29)$$

$$L_n(0.335) = 1, 2, 3, 4 \quad (4.4-30)$$

$$L_n(1.751) = 2, 3, 4, 5 \quad (4.4-31)$$

$$L_n(2.433) = 1, 2 \quad (4.4-32)$$

for the neutron exit channel, as dictated by:

$$|J_{\text{Na}^{21}} - S_n - 1| \leq L_n \leq J_{\text{Na}^{21}} + S_n + 1 \quad (4.4-33)$$

However, since all four levels are positive parity states the conservation of channel parity,

$$\Pi_f = (-1)^{L_n} \Pi_n \Pi_{\text{Na}^{21}}, \quad (4.4-34)$$

restricts the L_n values to:

$$L_n(\text{gnd}) = 0, 2 \quad (4.4-35)$$

$$L_n(0.335) = 2, 4 \quad (4.4-36)$$

$$L_n(1.751) = 2, 4 \quad (4.4-37)$$

$$L_n(2.433) = 2. \quad (4.4-38)$$

With these results we see that the presence of any centrifugal-barrier effects must influence the 0.335 and 1.751 levels equally. Thus the assumption of an equivalent compound reaction

contribution, to the 0.335 and 1.751 levels, is given foundation. In addition to this conclusion, if one couples the results of eqn. (4.4-35) and the realization that the stripping cross section is proportional to, $2J_f+1$, (eqn. 4.3-25) the following argument can be fabricated in support of the assumption that the ground state is formed wholly via the compound reaction mechanism.

With a ground state spin value of, $J_f = 3/2$, we see that the, $2J_f+1$, term would tend to retard the direct reaction formation of this state with respect to the 0.335 level. (Both levels have $\ell_p=2$ values, therefore, angular-momentum transfer arguments apply equally.) However, the allowability of a L_n (gnd) value of zero would tend to enhance the compound reaction formation of this state over that attributed to the 0.335 level. The complementary effect of these two restriction tends to validate the assumption.

Let us now turn our attention to the 2.433 level. Having excited only the $J=0$ level of the $|\frac{1}{2}+9\rangle$ band it is difficult to form any conclusions about the applicability of the,

$$\sum_{\ell j} \langle N \ell j | \frac{1}{2}+9 \rangle^2 = 1, \quad (4.4-39)$$

rule. However, realizing that highly excited states are generally characterized by $K \neq 0$, the selection rule of eqn. (4.4-17) would demand small spectroscopic factors for the

higher energy members of the $|\frac{1}{2}+9\rangle$ band. The value of, $\langle 20 \frac{1}{2} | \frac{1}{2}+9 \rangle^2 = 0.25$, for the 2.433 level is then probably quite realistic. This result then implies a strong direct reaction contribution to the formation of this level, which is further substantiated on the basis of angular-momentum transfer arguments. With a $L_n(2.433)$ value of 2, the compound reaction contribution is probably no greater than that attributed to the 0.335 and 1.751 levels. This would represent a 1.1% contribution.

One surprising feature about the 2.433 level is that, in spite of the fact that it corresponds to a single particle excitation, it is poorly represented by a spherically-symmetric shell model wave function (as indicated by a spectroscopic factor of only 0.25). It may be that the $K=\Omega$ selection rule is coming into play at this energy.

APPENDIX A

ASSOCIATED PARTICLE ANALYSIS: ASPANL

A-1 Introduction

ASPANL is a combined FORTRAN IV and MAP* language program written for an IBM 7040 computer. Its primary function is to compute the ratio, R , between the number of neutrons incident on the neutron detector to the number of neutrons produced in coincidence with a collimated flux of the kinematically associated particles. Fig. A-1 is a schematic outline of the experimental configuration.

The following quantities are required in the determination of R :

- (i) the size, shape, and spacing of the charged particle collimators: C2 and C3,
- (ii) the size and nature of the target: T,
- (iii) the size and shape of the incident beam collimator: C1,
- (iv) the distance of the neutron detector, D2, from the target, and
- (v) the kinematic inter-relationship of the reaction particles.

These variables interact in such a way as to produce a 2-dimensional distribution for the associated neutron flux. The quantity, R , is then determined by computing the ratio of the sum of this distribution over the

*Macro Assembly Program

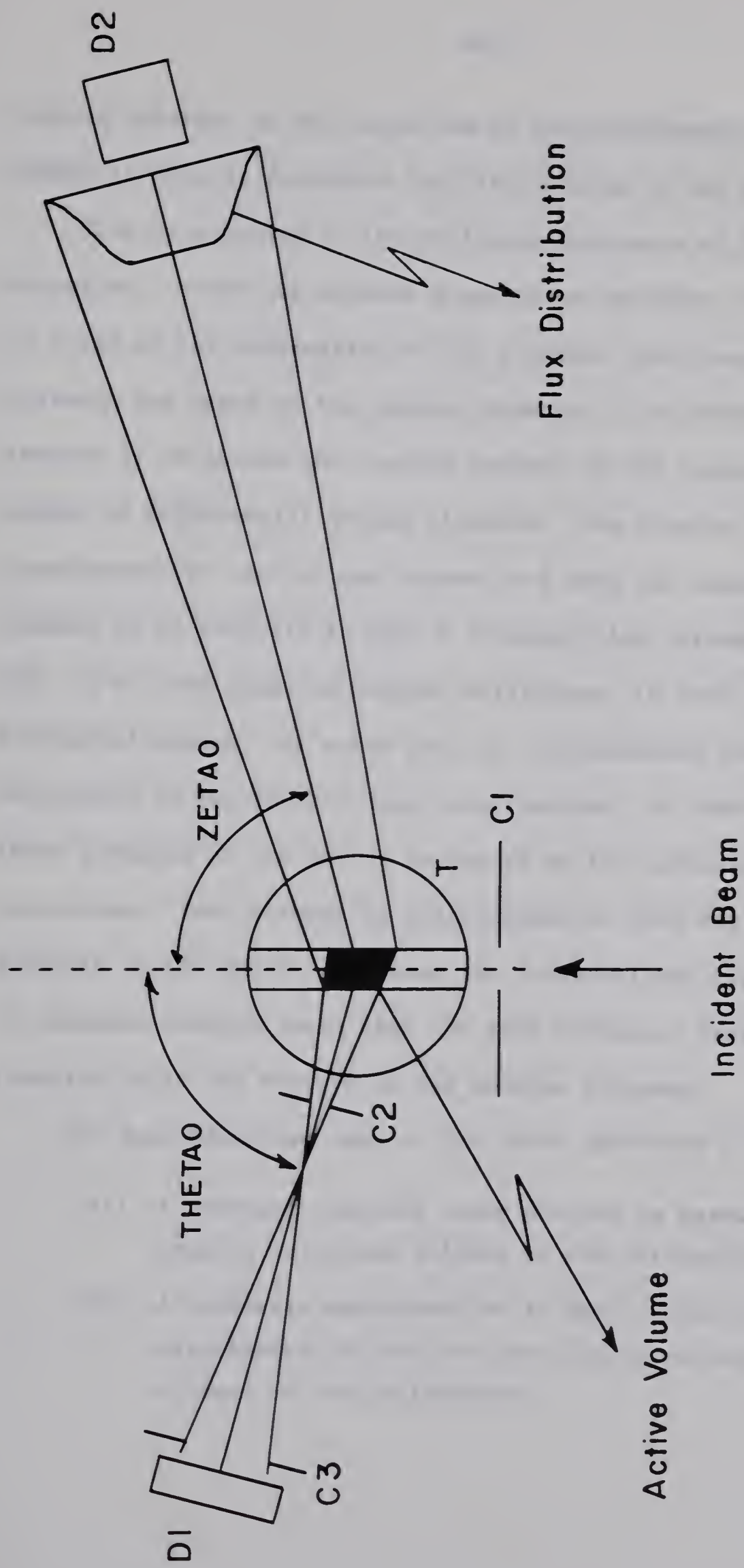


FIGURE A-1 Associated Particle Geometry

neutron detector to the total sum of the distribution. The basic task of ASPANL is then to determine the distribution of the associated neutron flux.

This is achieved by the following synthesis of the experimental situation. First one defines a matrix to represent the distribution and, in terms of the mathematics of the program, positions it at the same distance and angle as the neutron detector. The second initialization feature is to divide the "active volume" of the target into a specified number of differential volume elements. The program then computes the coordinates for each volume element and asks the question: for a given element is it possible to pass a straight line through collimators C2 and C3? If so, the range of angular variations, in both the vertical and horizontal planes, are noted and the corresponding kinematically associated variations in the neutron angle are computed. A count is then added to those elements of the matrix subtended by the associated neutron angular variations. Each element is interrogated in this way and the resultant contents of the matrix represent the 2-dimensional flux distribution. To minimize computational time the more redundant features of this interrogation cycle are written in MAP machine language.

The approximations made in the above synthesis of the problem are:

- (i) A constant reaction cross section is assumed across the angular variation allowed by the collimators.
- (ii) A quadratic approximation is made to the kinematic inter-relationship of the two particles over the angular variation allowed by the collimators.

- (iii) The number of matrix elements subtended by two different volume elements, which in turn subtend equal solid angles by the collimators, may differ due to the different angular orientations of the volume elements and the non-linear kinematic relationship between the two particles. Thus, as a consequence of adding a unit count to each matrix element subtended, the contribution to the neutron distribution will be greater for that volume element which subtends the greater number of matrix elements. Whereas, in reality, each volume element should contribute in a manner proportional to the solid angle subtended by the collimators.

These approximations are employed in an effort to minimize computational time and thus any small error that might be introduced is vindicated. In the case of point (iii) the point of view adopted by the program results in a significant saving in machine time, for one is then able to program the more redundant features of the interrogation cycle in fixed point.

The program is written with sufficient versatility to accommodate a number of different situations, viz, one can either specify the distance of the neutron detector or have it computed by an algorithm which positions it at such a distance that it just begins to subtend the constant flux portion of the distribution. In addition either a circular or rectangular aperture in collimator C1 can be specified. However, one is restricted to circular apertures only in collimators C2 and C3. Additional restrictions are that the target be of finite depth and that the face of the neutron detector be of circular geometry.

The primary application of the program has been to a circular gas target cell and the $D(d,n)He^3$ reaction. However, its application is easily extended to other reactions provided a similar target geometry is employed.

The above serves as a general introduction to the operation of ASPANL. For a more detailed description refer to (Bu 67).

A-2 Data Input

All input information to ASPANL is entered via punched cards. Each card contains a two digit control code and up to eight pieces of data. Each control code directs the program in compliance with the respective input information.

The following table describes the contents of each card. The format used throughout is:

FORMAT(1X,I2,1X,8E9.0)

TABLE A-1 INPUT DATA

Code	DATA
01	S1, S2, R1, R2, XSIZE, YSIZE, ZSIZE, DIAM
	<p>S1 = distance from the center of the target cell to the first collimator, C2 (inches)</p> <p>S2 = distance from the center of the target cell to the second collimator, C3 (inches)</p>

Table A-1 continued

CODE	DATA
	<p>R1 = aperture radius of the first collimator, C2 (inches)</p> <p>R2 = aperture radius of the second collimator, C3 (inches)</p> <p>XSIZE = length of target cell (inches)</p> <p>YSIZE = width of collimator C1 (inches)</p> <p>ZSIZE = height of collimator C1 (inches)</p> <p>DIAM = diameter of the neutron detector (inches) --variable DIAM is optional and need not be included.</p> <p>Control card 01 is to be entered if a rectangular aperture in collimator C1 is used.</p>
14	<p>S1, S2, R1, R2, XSIZE, YSIZE, DIAM</p> <p>S1 = distance from the center of the target cell to the first collimator C2 (inches)</p> <p>S2 = distance from the center of the target cell to the second collimator C3 (inches)</p> <p>R1 = aperture radius of the first collimator C2 (inches)</p> <p>R2 = aperture radius of the second collimator C3 (inches)</p> <p>XSIZE = length of the target cell (inches)</p> <p>YSIZE = aperture diameter of collimator C1 (inches)</p> <p>DIAM = diameter of the neutron detector (inches) --variable DIAM is optional and need not be included.</p> <p>Control card 14 is to be entered in exchange for control card 01 if a circular aperture in collimator C1 is used.</p>

Table A-1 continued

CODE	DATA
02	M1, M2, M4, Q, T1, LARGE
	<p> M1 = mass of the incident particle (A.M.U.) M2 = mass of the target particle (A.M.U.) M4 = mass of the primary particle (neutron) (A.M.U.) Q = Q value of the reaction (MeV) T1 = energy of the incident particle (MeV) LARGE = a variable specifying that in the case of a double valued reaction the higher (or lower) energy of particle 3 (He^3) is used in evaluating the neutron flux distribution, i.e. LARGE \geq -0.001 : higher energy is used. LARGE $<$ -0.001 : lower energy is used. LARGE unspecified : higher energy is used. </p> <p>Control card 02 need not be given if control card 10 is given.</p>
03	PRES, TEMP, CURRNT
	<p> PRES = pressure of gas within the target cell (cm Hg) TEMP = temperature of gas within the target cell ($^{\circ}\text{C}$) CURRNT = the beam current incident on the target cell (μamps) </p> <p>If this card is entered, the target thickness is computed assuming a deuterium target.</p> <p>See also control cards 05 and 08.</p>
04	NUMPTS
	<p>NUMPTS = the number of differential volume elements into which the "active volume" is to be divided. From this number the incremental distances DELX, DELY, DEYZ are computed.</p> <p>NUMPTS is set to 500.0 if neither control card 04 or 07 is specified.</p>

Table A-1 continued

CODE	DATA
05	<p>THETA0, SIGMA</p> <p>THETA0 = the central angular position of the collimator system C2 and C3 with respect to the beam direction (degrees)</p> <p style="text-align: center;">$5^{\circ} \leq \text{THETA0} \leq 175^{\circ}$</p> <p>SIGMA = the differential cross section of the reaction corresponding to particle 3 (He^3) being located at THETA0 (mbarns/sterd.)</p> <p>If control card 03 is entered, a reaction count rate is computed assuming the D(d,n)He^3 reaction.</p> <p>If control card 03 is not entered, SIGMA is ignored and the parameter UNTCNT is set equal to unity.</p>
06	<p>(BLANK)</p> <p>Control card 06 causes the first 78 characters of the next card to be accepted as title information.</p>
07	<p>DELX, DELY, DELZ</p> <p>DELX = incremental distance along length of active volume (inches)</p> <p>DELY = incremental distance along width of active volume (inches)</p> <p>DELZ = incremental distance along height of active volume (inches)</p> <p>This card overrides control card 04.</p>
08	<p>UNTCNT</p> <p>UNTCNT = the count rate per cubic inch per steradian within the target</p> <p>This card overrides the value of UNTCNT calculated from the data entered via control cards 03 and 05.</p>

Table A-1 continued

CODE	DATA
09	DN
	<p>DN = the distance from the center of the target cell to the neutron detector (meters)</p> <p>If DN is not entered, it is computed subject to the condition that the neutron detector just begin to subtend a constant flux.</p> $1.016 \leq ON \leq 6.0 \text{ (m)}$ <p>If DIAM is not given or if all six angles are given, via control card 10, then DN is set to the longest value (6.0 m) if it is not specified.</p>
10	THETAP, THETAO, THETAM, ZETAP, ZETAO, ZETAM
	<p>THETAP = minimum angle allowed by collimator C2 and C3 (degrees)</p> <p>THETAO = central angle of collimators C2 and C3 (degrees)</p> <p>THETAM = maximum angle allowed by collimators C2 and C3 (degrees)</p> <p>ZETAP = the neutron angle kinematically associated with THETAP (degrees)</p> <p>ZETAO = the neutron angle kinematically associated with THETAO (degrees)</p> <p>ZETAM = the neutron angle kinematically associated with THETAM (degrees)</p> <p>All these angles, except THETAO, are normally calculated from the data entered via control card 01 or 14.</p> <p>The data entered via control card 10 overrides all previously calculated values.</p>
11	NORM
	<p>NORM = a variable whose magnitude determines whether the matrix representing the neutron flux distribution is normalized with respect to count rate on the basis of the computed target thickness, cross section, and beam current.</p>

Table A-1 continued

CODE	DATA
	NORM > -0.001 : the scatter diagram is normalized NORM unspecified : the scatter diagram is normalized NORM <u>≤</u> -0.001 : the scatter diagram is not normalized
12	(BLANK)
	This control code terminates data input and initiates execution of the run.
13	(BLANK)
	This control code terminates the program by calling SUBROUTINE EXIT

The data cards are to be entered in order of increasing code number (except for code 14 which replaces 01) and all parameters, except those on control cards 07, 09, and 11 remain unchanged from run to run. Table A-2 is a sample listing of input data illustrating the need for only a portion of the available input cards.

The three cards following control card 13 form the calling sequence for AUTO PLOT, a library plotting program written by J. F. Easton (Ea 64). Its relationship to ASPANL is discussed under heading A-3 Data Output.

TABLE A-2 SAMPLE INPUT DATA

\$ENTRY

14 0.60 4.60 0.038 0.100 1.00 0.182 3.50

02 2.014740 2.014740 1.008986 3.266 2.96

03 3.50 20.0 1.5

04 8000.0

05 31.2 3.50

06

D(D,N)HE-3 E 2.96 THETA 31.2 MARCH 16 1967 RUN NO. 8

09 2.012

12

13

\$EXECUTE AUTOPT

PLOT ALL

PLOT DONE

A-3 Data Output

The output of each run consists of a data sheet, a scatter diagram, and a graphical plot, represented respectively by Figs. A-2, A-3, and A-4.

The first portion of the data sheet is a kinematic analysis of the reaction. The quantities M1, M2, M3, and M4 are respectively the masses of: the incident particle, the target particle, the associated particle (He^3), and the primary particle (n) with T1, T3, and T4 their respective energies. The three angles listed are respectively: the minimum, central, and maximum angles allowed by collimators C2 and C3. In the event of a double valued reaction the corresponding angles and energies of the lower energy neutron group are printed alongside the angles and energies of the higher energy group.

The next portion under the heading "Given Data" is just a restatement of some of the input data.

The quantities under the heading "Computed Data" includes: a statement of the number of volume elements employed, based on the incremental values of DELX, DELY, and DELZ; a statement of the time taken to compute the flux distribution; and an evaluation of the quantity UNTCNT, i.e. the count rate per cubic inch per steradian within the target.

The final portion under the heading "Scatter Diagram Data" contains the important results of the program. The quantities XNDEL and YNDEL are respectively the width and height of the matrix elements making up the flux distribution. These quantities, when multiplied by the dimensions

M1= 2.0147400 M2= 2.0147400 M3= 3.0169864 M4= 1.0089860 AMU. T1= 2.96 Q= 3.2660 MEV. M3 COMPUTED FROM Q

COLLIMATOR ANGLES CORRESPONDING ANGLES KINETIC ENERGY MEV
ASSOCIATED PARTICLE M3 PRIMARY PARTICLE M4 T3 T4

CENTRAL 29.224 DEGREES 104.398 DEGREES 3.5393 2.6867
31.200 100.233 3.4063 2.8198
33.176 96.177 3.2683 2.9577

*** GIVEN DATA ***

COLLIMATORS DISTANCE TO FIRST 0.600 DISTANCE TO SECOND 4.600 RADIUS OF FIRST 0.038 RADIUS OF SECOND 0.100 INCHES
TARGET (CIR) DIAMETER OF BEAM 0.182 LENGTH OF BEAM 1.000 INCHES
PRESSURE (CM-HG.) 3.5 TEMPERATURE (DEG. C) 20.0 I BEAM (UAMPS) 1.5000 XSECT.(MB) 3.500
TARGET THICKNESS (UGM/CM**2) 19.598

DELX= 1.0446816 E-02 DELY= 8.3945601 E-03 DELZ= 4.7763569 E-03
ABOVE INCREMENTS IN TARGET WERE COMPUTED TO GIVE APPROX. 8000 POINTS TO BE USED IN WHOLE VOLUME.

DIAMETER OF PRIMARY COUNTER 3.500 (INCHES) DISTANCE TO PRIMARY COUNTER 2.012 (METERS) GIVEN

*** COMPUTED DATA ***

NUMBER OF POINTS USED IN THE HALF VOLUME 4272
TIME TAKEN IN SUBROUTINE SPREAD 20.287 (MIN.)
COUNT RATE PER IN**3 PER STERADIAN IN TARGET 7.379939E 06

*** SCATTER DIAGRAM DATA ***

TOTAL WIDTH OF SCATTER DIAGRAM 12.4818106 XNDEL= 1.2358228 E-01
TOTAL FULL HEIGHT OF SCATTER DIAGRAM 10.8092198 YNDEL= 1.0702198 E-01

ONE COUNT IN SCATTER DIAGRAM 1 REPRESENTS PRIMARY COUNT RATE OF 6.5158687 E-06
CENTRAL COUNT IN SCATTER DIAGRAM 3680 2.3978397 E-02 PER IN**2= 1.8129714 E 00
COUNTS NOT INCLUDED IN SCATTER DIAGRAM 0
TOTAL COUNTS 13759524 8.9655252 E 01

INTEGRATED COUNT IN THE PRIMARY DETECTOR 1.735487E 01
RATIO OF TOTAL COUNTS TO THOSE IN THE DETECTOR 0.19357341

SOLID ANGLE SUBTENDED BY PRIMARY DETECTOR 1.5333337E-03
SOLID ANGLE OF WHOLE FLUX ASSUMING ELLIPSE 1.589948E-02
RATIO OF SOLID ANGLES 0.09643946

[illegible]

FIGURE A-3 SCATTER DIAGRAM

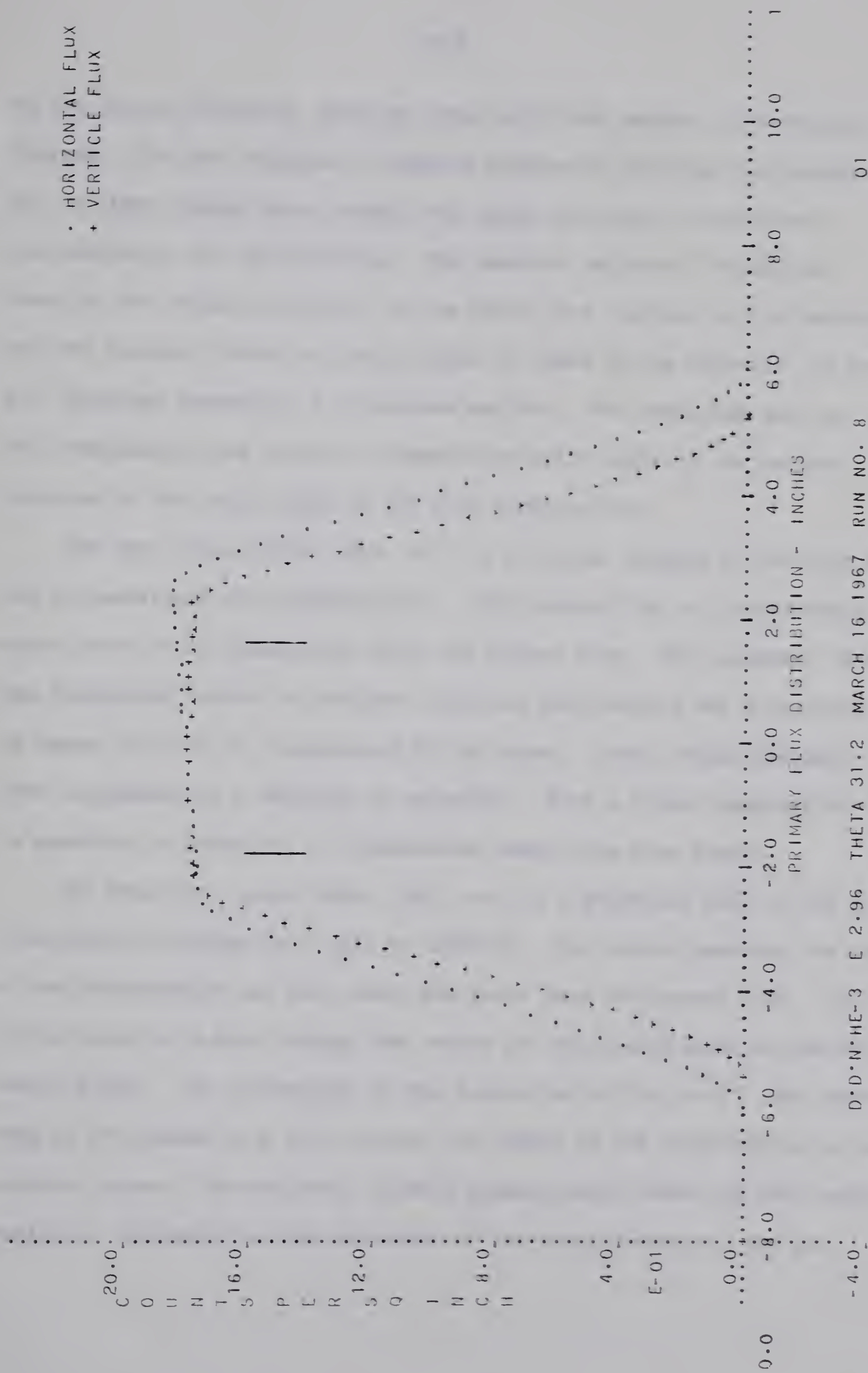


FIGURE A-4 FLUX CONTOUR

of the matrix (101x101), give the total width and height of the scatter diagram. The next sequence of numbers relates to the flux distribution and outlines, among other things, the total count rate (counts/sec) represented by the distribution. The quantity entitled "Integrated Count in the Primary Detector" is the count rate incident on the detector, and the quantity "Ratio of Total Counts to Those in the Detector" is the all important parameter, R, discussed earlier. The remaining data is self explanatory and serves to compare the solid angle of the neutron detector to the solid angle of the flux distribution.

The next output sheet (Fig. A-3) is a scatter diagram of one-half of the 2-dimensional flux distribution. Only one-half of the distribution is shown since it is symmetrical about the bottom line. The statement "Matrix Was Normalized" refers to the fact that the distribution was normalized to an upper limit of 10, represented by the stars. Lower valued integers then correspond to a decrease in intensity. With a little imagination it is possible to visualize a 3-dimensional image from this figure.

The remaining output sheet (Fig. A-4) is a graphical plot of the flux distribution obtained by a call to AUTO PLOT. The x-axis measures the radius of the distribution and the y-axis the count rate per square inch. The dotted curve is a plot through the center of the distribution in the horizontal plane. (It corresponds to the bottom row of Fig. A-3.) The curve made up of crosses is a plot through the center of the distribution in the vertical plane. The two bars, located symmetrically about the zero radius position, correspond to the placement of the neutron detector and are

determined internally in accordance with the value of DN, the distance of the neutron detector from the target. It will be noted that the title entered via control card 06 appears on each data sheet.

BIBLIOGRAPHY

- Aj 61 F. Ajzenburg-Selove et al; Phys. Rev. 124, (1961), 1548.
- Aj 66 F. Ajzenburg-Selove; Nucl. Phys. 78, (1966), 1.
- Al 60 W. D. Allen; "Flat Response Counters", Chapter 3I; Fast Neutron Physics; edited by J. B. Marion, (Interscience, 1960).
- Al 65 J. P. Allen; Doctoral Dissertation, Yale University, 1965, (unpublished).
- Am 65 O. Ames et al; Phys. Rev. 137, (1965), B1157.
- Ar 63 S. E. Arnell and S. Sterner; Arkiv For Fysik 25, (1963), 531.
- Au 64 N. Austern et al; Phys. Rev. 133, (1964), B3.
- Ba 64 R. H. Bassel; "Some Applications of the Distorted Wave Approximation for Direct Nuclear Reactions", ORNL Report P-144-IOF3, (1964).
- Be 61 R. E. Benenson and L. J. Lidofsky; Phys. Rev. 123, (1961), 939.
- Be 61 P. R. Bevington et al; Phys. Rev. 121, (1961), 871.
- Bh 62 K. H. Bhatt; Nucl. Phys. 39, (1962), 375.
- Br 60 J. E. Brolley and J. L. Fowler; "Monenergetic Neutron Sources: Reactions with Light Nuclei", Fast Neutron Physics; VI, pp 73; edited by J. B. Marion; (Interscience 1960).
- Bu 67 M. B. Burbank and J. F. Easton; "Associated Particle Analysis: ASPANL"; Nuclear Research Center,

University of Alberta, (1967).

- Ch 63 B. E. Chi and J. P. Davidson; Phys. Rev. 131,
(1963), 366.
- Da 66 W. G. Davies; Ph.D. Thesis, University of Alberta,
1966, (unpublished).
- En 62 P. M. Endt and C. Van der Leun; Nucl. Phys. 34,
(1962), 1.
- Ev 63 F. Everling; Nucl. Phys. 40, (1963), 670.
- Fi 66 A. A. Fife; M. Sc. Thesis, University of Alberta,
Appendix C, 1966, (unpublished).
- Ge 66 D. A. Gedcke; "Modification to T.M.C. Analyser",
Nuclear Research Center, University of Alberta,
(April 1966).
- Ge 66a D. A. Gedcke; "T.M.C. Kicksorter Memory Routing
Unit", Nuclear Research Center, University of
Alberta, (Aug. 1966).
- Ge 67 D. A. Gedcke and W. J. McDonald; "Design of the
Constant Fraction of Pulse Height Trigger for
Optimum Time Resolution", Nuclear Research Center,
University of Alberta, (Aug. 1967).
- Gi 65 W. R. Gibbs; Nucl. Phys. 62, (1965), 548.
- Go 61 M. D. Goldberg et al; Phys. Rev. 122, (1961), 1510.
- Gr 66 T. B. Grandy and D. A. Gedcke; "Tepel's Peak
Fitting Program: ANNELIESE", Nuclear Research
Center, University of Alberta, (Dec. 1966).

- Gr 67 T. B. Grandy; Ph.D. Thesis, University of Alberta, 1967, (unpublished).
- Gr 67a T. B. Grandy; "Relativistic Kinematics", Nuclear Research Center, University of Alberta, (1967).
- Ho 61 A. M. Hoogenboom; Rev. of Scientific Instr. 32, (1961), 1395.
- Ho 65 A. J. Howard et al; Phys. Rev. 139, (1965), B1135.
- Ho 67 A. J. Howard et al, Phys. Rev. 157, (1967), 1022.
- Ja 65 R. Jahr and G. Mairle; Nucl. Phys. 70, (1965), 383.
- Ke 64 I. Kelson and C. A. Levison; Phys. Rev. 134, (1964), B269.
- La 66 "Nuclear Reaction Q-Values"; Lawrence Radiation Laboratory, UCRL-16964, (July 1966).
- Ma 56 J. B. Marion et al; Phys. Rev. 103, (1956), 676.
- Ma 64 B. E. F. Macefield; "A Compilation of Computer Codes Useful in Nuclear Structure Physics", BNL-9108, (1964).
- Mc 67 W. J. McDonald and D. A. Gedcke; "Time Resolution Studies on Large Photomultipliers", Nuclear Research Center, University of Alberta (April, 1967).
- Ob 66 A. W. Obst; M.Sc. Thesis, University of Alberta, 1966, (unpublished).
- Pe 65 E. F. Pessoa et al; Nucl. Phys. 68, (1965), 337.
- Po 67 J. G. Pronko et al; Nucl. Phys. A94, (1967), 561.
- Re 66 W. B. Reid and R. H. Hummel; Can. Nuclear Tech. (Jan.-Feb. 1966).

- Ro 66 L. Rosen; "Elastic Scattering of Polarized Nucleons",
Proceedings of the 2nd International Symposium
on Polarized Phenomena of Nucleons; Birkhäuser
Verlag Basel Und Stuttgart, (1966); p 278.
- Sa 58 G. R. Satchler; Annals of Physics 3, (1958), 275.
- Ta 60 M. Takeda; J. of Phys. Soc. of Japan 15, (1960),
557.
- Te 66 J. W. Tepel; Nucl. Instr. and Methods 40, (1966),
100.
- Va 64 C. Van der Leun and W. L. Mouton; Physica 30,
(1964), 333.
- Wi 63 D. L. Wieber; Nucl. Instr. and Methods 24, (1963),
269.

B29869